FINAL REPORT

IWRC-USGS PROJECT TITLE

"Characterization of Critical Shear Stresses and

Bank Material Erosion Rates on Gravelly Stream Banks"

Report Title

A Physically-Based Bank Erosion Model for Composite River Banks: application to Mackinaw River, Illinois

(CFP 1-486445-191100 USGS IWRC 2011)

Submitted by: **David M. Waterman, Research Assistant**
Marcelo H. Garcia, Principal Investigator
Ven Te Chow Hydrosystems Laboratory
Civil and Environmental Engineering
University of Illinois at Urbana-Champaign
301 N. Mathews Ave., Urbana, IL 61801

Prepared for: **Illinois Water Resource Center**
388 NSCR, MC-635
1101 W. Peabody Drive
Urbana, Illinois 61801 USA

Date: May 12, 2013

Abstract:

Meandering river migration over large spatial and temporal scales has traditionally been numerically simulated using a bank erosion submodel that calculates the eroding bank migration rate as the product of the near-bank excess flow velocity and a dimensionless migration coefficient. The latter value is an empirical parameter calibrated to historical observations. In efforts to improve upon the traditional model, recent research has followed two approaches: (a) provide a means of estimating the dimensionless migration coefficient based on field measurements; and (b) discard the traditional migration coefficient approach to develop a bank erosion submodel based on the actual formulations that dictate fluvial erosion rates and mass failure which determine bank migration. The latter physics-based approach was recently implemented into the numerical model RVR Meander developed by the Ven Te Chow Hydrosystems Laboratory at the University of Illinois in Urbana-Champaign (Motta et al, 2012a); however, the governing equations used for fluvial erosion strictly apply only to banks comprised of cohesive soils. In that formulation the fluvial erosion rate is linearly dependent on the excess boundary shear stress. This study explores whether a similarly simple formulation can describe in a gross sense the migration of river banks comprised entirely of non-cohesive soil or composite banks consisting of non-cohesive soil at the base overlain by cohesive soil. Numerical modeling of both fluvial erosion and shallow avalanche mass failures that occur simultaneously during non-cohesive bank deformation reveal that the bank migration rate is strongly non-linear with respect to the boundary shear stress (exponent greater than 1) when considering non-cohesive bank materials. A methodology is described for developing a site-specific non-cohesive bank erosion submodel that is valid and computationally practicable over the desired large spatial and temporal scales relevant to models such as RVR Meander. The new methodology allows issues such as flow regime modifications to be incorporated to change the model parameters, which was not possible using the traditional empirical approach. The numerical modeling performed in this study also provides fundamental insights into deformation of non-cohesive river banks: it demonstrates that high flow events tend to cause bank slope reduction, with lower flow events tending to rejuvenate the steepness of the bank; it quantifies the importance of prior erosional history in influencing bank migration rates; and it quantifies the feedback of basal armoring on deformation of the unarmored region.

Table of Contents

1. Introduction

River geometry is formed and adjusted based on feedbacks between flow hydraulics, sediment transport, and channel geometry / composition; realistic morphodynamic simulation requires the modeling and coupling of all these facets. Fully mechanistic numerical models that include three-dimensional (3D) hydrodynamics and movable boundaries (e.g., Rüther and Olsen, 2007) are in their infancy and cannot currently be practically applied to the large spatial and temporal scales commonly of interest to engineers and geologists. Therefore, simplifying assumptions are necessary to model river systems at the desired scales; the simplifications must capture the essential physics of the system without being so complex as to be computationally impractical to implement. The primary approach used in the past by meandering river researchers has been the classic model developed independently by Hasegawa (1977) and Ikeda et al (1981), which implements the following submodels: (a) a 2D depth-averaged hydrodynamics submodel with constant channel width per Engelund (1974), which can be linearized to yield an analytical solution for flow velocity; (b) simplified bed evolution submodel with scour as a function of local curvature; (c) a simplified bank erosion submodel. The bank erosion submodel is the focus of the current study; in keeping with the terminology included in Motta et al (2012a), the bank erosion submodel of Hasegawa (1977) and Ikeda et al (1981) is referred to as the Migration Coefficient (MC) approach. Per the MC approach, the near-bank excess velocity (u') is defined as the difference between the near-bank velocity and the reach-averaged velocity. The bank erosion rate in the direction normal to the channel centerline is calculated as the near-bank excess velocity multiplied by a migration coefficient (E).

Theoretical justification for the usage of near-bank excess velocity u' in a bank erosion submodel was provided by Hasegawa (1989); however, in that study it was found that the migration coefficient E theoretically contained elements of both bank properties (e.g., bank slope, bank height, friction angle of bank material) and flow properties (bed/bank shear stresses, intermittency of bankfull flow). Past research implementing the MC formulation has generally attempted to correlate E with bank conditions alone. Wallick et al (2006) identified variations in E based on bank erosion into distinct geological formations; and Constantine et al (2009) provided evidence of a correlation between E and fluid shear resistance of bank material determined through a submerged-jet test. The attempts to provide physical correlations to the parameter E is an important research topic, however, at present the only accurate method of estimating E remains to be through calibration with historical migration data (Johannesson and Parker, 1985; Abad and Garcia, 2006). Such an approach has serious shortcomings; for engineering purposes, a model needs to be able to evaluate changes in flow regime or other physical changes to the river system, and calibration to historical conditions has limited relevance under those circumstances.

The shortcomings due to the empirical nature of the MC formulation have generated the need to provide a more physical basis for a bank erosion submodel. The Ven Te Chow Hydrosystems Laboratory at the University of Illinois at Urbana-Champaign has been actively involved in this effort. The computer program RVR Meander originally coupled a 2D hydrodynamics submodel with the MC formulation bank erosion submodel (Abad and Garcia, 2006); the program was extended by Motta et al (2012a) to implement a more physically-based bank erosion submodel using the approach of the U.S. Department of Agriculture model CONCEPTS (Langendoen and Simon, 2008; Langendoen et al, 2009). The modified RVR Meander-CONCEPTS model accounts for fluvial erosion and mass failure of bank material. The fluvial erosion rate is based on a well-established formula for cohesive bank material, where the erosion rate is linearly proportional to the excess boundary shear stress per Partheniades (1965) and Arulanandan et al (1980). Because of the simplicity of the fluvial erosion formulation, it can be implemented in a numerical model with minimal computational expense relative to the MC approach. This formulation requires two parameters, the critical bank shear stress (τ_c) and the constant of proportionality M, referred to as an erosion-rate coefficient. The submerged jet-test (Hanson, 1990; Hanson and Cook, 2004) provides a promising means of estimating these parameters. However, it remains unclear whether the linear relationship between fluvial erosion rate and excess shear stress that applies to cohesive banks can be applied to non-cohesive bank materials, where the physics of bank deformation are considerably different.

In the current study, a new method is described for developing and parameterizing a bank erosion submodel for non-cohesive river banks. The specific type of bank considered is a composite bank containing an upper layer of cohesive soil (silt and clay) overlying a lower layer of non-cohesive soil (sand and gravel), such as exists in a reach of interest on the Mackinaw River in Illinois. The new method is a process-based approach utilizing known relationships for sediment transport and mass failure; it utilizes an effective discharge approach for determining the effects of flow regime. Using this new method, parameters can be estimated in the absence of historical plan form data and parameters can be modified based on changes in the river system. This is a substantial improvement from parameterization based solely on calibration to historical migration conditions. Although the processes described apply to composite banks, the general approach to parameterization can be extended to other bank types for which the processes of fluvial erosion and mass failure are different.

2. Characteristics of Composite River Banks

Alluvial rivers meander through floodplains formed of their own sediment. Much of the floodplain deposits are channel bars that were left in place as the river migrated. The channel-bottom and bar deposits are generally non-cohesive sediment (sand and gravel) and tend to be coarser-grained at the base and finer-grained near the surface. Overlying the bar deposits is finer grained material deposited during overbank flow events; the overbank deposits generally consist of a mixture of fine sand, silt, and clay. The eroding bank of a river is classified as a composite river bank when it is eroding into such floodplain materials. During migration, the non-cohesive basal layer tends to undergo fluvial erosion and the cohesive upper layer tends to undergo mass failure due to destabilization by undercutting (Thorne and Tovey, 1981).

Non-cohesive sediments deposited recently tend to be loosely packed and cannot remain standing at steep angles when submerged. However, non-cohesive floodplain deposits that were emplaced many centuries ago can undergo densification and compression over time, increasing the interlocking among particles and allowing these deposits to stand at steeper angles. Examples of the latter condition are provided by Thorne and Tovey (1981), Powell and Ashworth (1995), and Darby et al (2007). When such material collapses, it loses its structure and reverts to the properties of the loosely packed recent deposits. Following the terminology of Leroueil and Vaughan (1990), the densely packed deposits are referred to as "structured" and the loosely packed deposits are referred to as "unstructured". A structured deposit has different mechanical behavior in situ than a sample, due to disturbance of the structure during sampling. A schematic diagram of a typical composite river bank is shown in Figure 1.

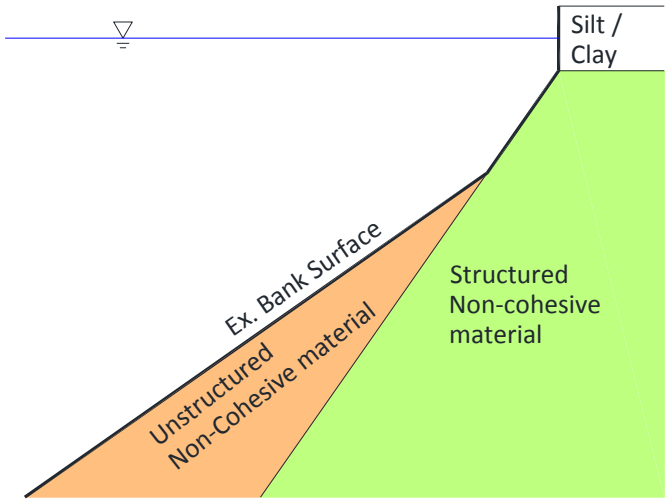

Figure 1: Conceptual Cross-Section of a Composite River Bank (after Thorne and Tovey, 1981).

One feature of composite banks that can mitigate fluvial erosion of the lower non-cohesive layer is basal armoring. The armoring can be naturally generated by a number of causes: (a)

failed blocks of the upper cohesive layer roll to a stable position on the lower slope, commonly toward the base (Thorne, 1982; Wood et al, 2001; Parker et al, 2011); (b) related to slump block armoring, silt and clay can deposit in the matrix of the non-cohesive layer, originating from eroding slump blocks or suspended sediment from the river water column deposited during the tail of a hydrograph; (c) during fluvial erosion and shallow mass failures of the non-cohesive basal layer, the finer grains can be winnowed, increasing the median diameter of the unstructured basal sediment, thus increasing the boundary shear stress required to mobilize the material (Darby et al, 2002); (d) large woody debris can become emplaced along the bank base and cause coarse sediment to accumulate immediately upstream. A basis for item (b) is the research of Mitchener and Torfs (1996), who found that the addition of 30% mud into a sandy bed increases the critical shear stress (τ_c) by approximately ten times relative to sand only, with a maximum τ_c occurring at 50 to 70% sand by weight; similar findings were demonstrated by Panagiotopoulos et al (1997). Kothyari and Jain (2008) found that adding clay to a gravel bed increased τ_c by approximately three times relative to gravel only.

A field site on the Mackinaw River in north-central Illinois has composite banks and also displays some of the characteristic armoring features. An aerial photograph of the field site is provided in Figure 2, and photographs are provided in Figures 3 through 5.

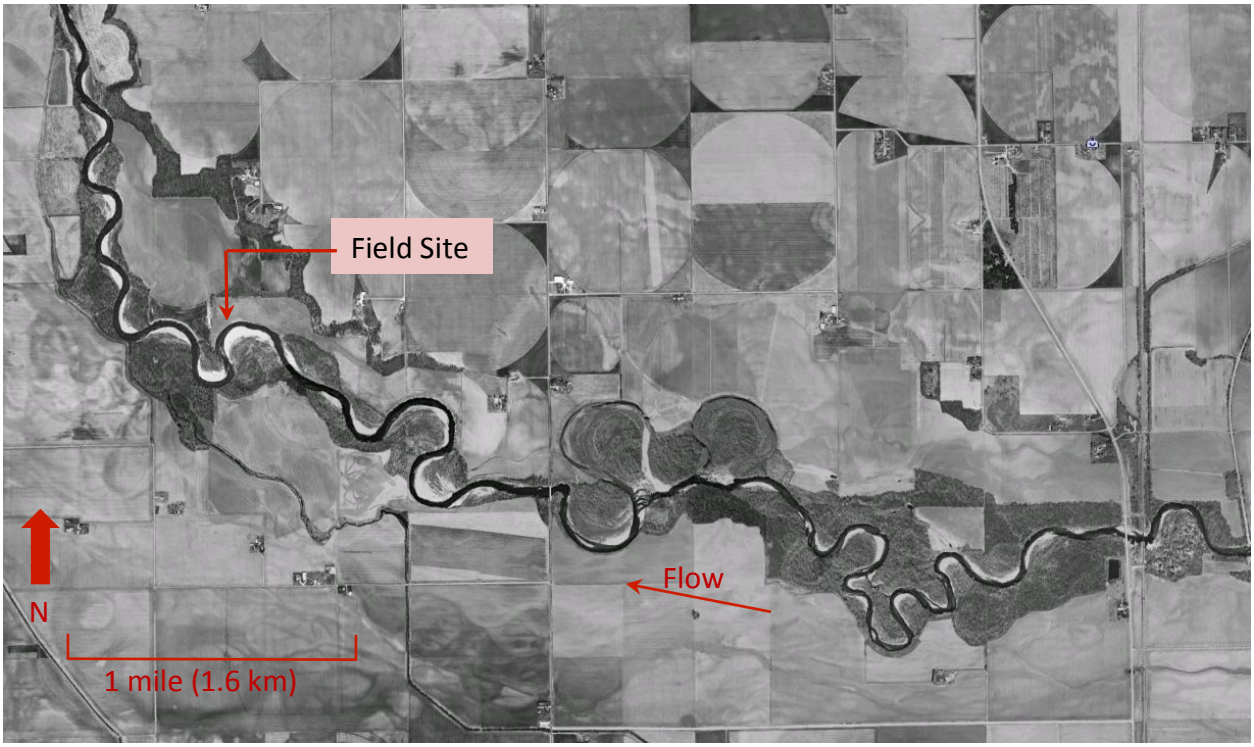

Figure 2: 2005 Aerial Photograph of Mackinaw River (Source: Google Earth)

Figure 3:
A photograph looking upstream at the eroding river bank at the field site shown in Fig. 2. The bank profile is distinctly concave. Unstructured non-cohesive sediment (gravel) is present at the base of the bank at a mild slope angle.

Figure 4:
A view of the same general area from the bottom of the slope. Silt and clay has deposited in the gravelly matrix of the unstructured sediment at the base.

Figure 5:
A view of the distinct contact between the fine-grained cohesive upper layer and the coarse-grained non-cohesive lower layer. The upper layer stands nearly vertical.

2.1 Relevant Angular Properties

The properties of a soil are commonly expressed in terms of friction angle, angle of repose, pivoting angle, and angle of initial yield, among other terms. Unfortunately, in the sediment transport literature, these terms are often used interchangeably and the intended meaning in a particular usage is not always clear. Some of the variables represent mass properties of the soil, which are of most relevance in geotechnical engineering analysis; other variables represent particle properties, which are of most relevance to sediment transport analysis. Various angular properties are necessary for the modeling of the present study, and so a discussion of the meanings is warranted.

The mass angle of repose (θ_{rm}) is a mass property of the soil which dictates the angle at which an avalanched group of particles will come to rest. The mass angle of repose was quantified in the experiments of van Burkalow (1945). Loose sand was placed in a box, one of the vertical sides of the box was lifted, and the sand spilled out, coming to rest at a characteristic angle. From those experiments, values of θ_{rm} centered in a narrow distribution around 33 degrees. In the context of the current analysis, a mass failure or shallow avalanching of non-cohesive bank material should result in particles that come to rest somewhere downslope at the mass angle of repose. The value θ_{rm} = 33° is used in this analysis.

The particle angle of repose (θ_{rp}) is the maximum slope on which a particle can remain at rest before tipping due to its own weight or sliding. For a theoretical analysis of particle tipping due to fluid drag on a flat bed, the tangent of θ_{rp} represents the ratio between the moment arms of the gravitational resistive force directed vertically and the fluid drag force directed horizontally about the fulcrum of tipping (the point of contact between the particle and its neighbors). The term particle angle of repose in this respect is equivalent to the term pivot angle used by Li and Komar (1986). The particle angle of repose was quantified in the experiments of Eagleson and Dean (1959), Miller and Byrne (1966) and Kirchner et al (1990), in which a single particle was randomly placed on a plate containing glued particles, and the plate was tilted until the particle motion was initiated. Those studies found that θ_{rp} was considerably larger than the 33° mass angle of repose. The relation for θ_{rp} was found to vary based on: (a) the ratio between grain size of the fixed bed particles versus grain size of the loose particle; and (b) grain shape. In the experiments using a fixed bed of spherical particles and a loose spherical particle of the same size, θ_{rp} was found to equal 48.6°; with natural sand resting on a bed of equal-sized sand, θ_{rp} exceeded 60°. Kirchner et al (1990) experimentally found the same general trends in the mean as the previous experimenters, but found that the distribution under each experimental condition was very broad. When comparing analytical results to experimental results regarding initiation of sediment

motion, Wiberg and Smith (1987) concluded that the relevant particle angle of repose in a force balance should be closer to the 60° of Miller and Byrne (1966) than the 33° commonly accepted as the relevant angle of repose. Using the theoretical approach of Ikeda (1982), curves with various assumed θ_{rp} were compared with Shields' empirical data in Garcia (2008), and a good fit was found with θ_{rp} = 60°. There is still not a general consensus on the correct value to use for θ_{rp}, but the data suggests that under most circumstances the parameter should be at least 45° for unstructured (loosely packed) non-cohesive sediment. For structured non-cohesive sediment, θ_{rp} would be roughly equal to the maximum bank slopes observed in the field under submerged conditions per Millar and Quick (1993) and Millar (2000). θ_{rp} is a required parameter utilized in the modeling of the current study to quantify mobilization of particles on a bank side slope. The value θ_{rp} = 50° is used in this analysis.

A mass failure of non-cohesive granular material can occur in two general forms: (a) shear failure along a large-scale failure plane in which all particles begin moving simultaneously; or (b) a grain-flow avalanche in which a chain reaction occurs with a perturbation propagating outward as grains are sequentially destabilized (e.g., Daerr and Douady, 1999). No distinction is made between the two types in the current modeling effort, as the initial condition to initiate the mass movements and the end condition after motion has ceased are effectively the same. The two relevant angles in an analysis of mass failure are the friction angle (Φ) and the angle of initial yield (Φ_i). These are discussed separately below.

(i) The friction angle (Φ), also known as the angle of internal friction, is a mass property of the soil; it indicates the increase in the frictional resistance to shearing with increased applied normal force. For loose uniform round sand under small loadings, the friction angle is approximately 33°; when uniform sand is densified, that angle can be as high as 45°; for packed gravels and well-graded (poorly sorted) sandy gravels, it can be even higher (Terzaghi et al, 1996). Because of the high friction angles of non-cohesive materials, the shear strength increases more rapidly with depth than the shear stress, and consequently mass failures tend to occur as shallow failures near the surface. Using the Mohr-Coulomb strength criterion, an unconfined soil with no cohesion has a factor of safety equal to 1 (gravitational driving force equal to frictional resisting force) when the surface slope is equal to Φ. A shear failure plane will occur along a slope equal to Φ.

(ii) The angle of initial yield (Φ_i) per Allen (1970) is the maximum slope at which a pile of grains will stand before a mass of grains avalanches down the slope. Allen (1970) observed that before avalanching the downstream face of a dune steepens beyond both the failure plane angle (Φ) and the angle at which the failed material comes to rest (θ_{rm}). The angle of initial yield Φ_i is a mass property of the soil and is closely

related to the friction angle Φ; it reflects the experimental observation that failure of a steep slope does not instantaneously occur at a factor of safety (FS) exactly equal to 1 associated with a surface standing at a slope equal to the friction angle Φ. While failure may be considered impending at FS = 1, the probability of failure within a given timeframe increases as the factor of safety is reduced. The angle of initial yield Φ_i quantifies the probabilistic nature of this phenomenon under the small time scales relevant for a continuously evolving bank. Φ_i will always be greater than equal to Φ, but is not likely to deviate far from Φ. Experiments to determine Φ_i were performed by Allen (1970) and Carrigy (1970) using a rotating drum partly filled with grains. Carrigy (1970) found a Φ_i value equal to 37° for loose grains; Allen (1970) compacted grains by vibration and found Φ_i values that ranged from 44° to 53° depending on the grain size. The value Φ_i = 40° is used in this analysis; this represents natural material that is not as loose as laboratory sand, but without the interlocking of an intentionally compacted sample.

As shown in Figure 6 below, an avalanche is modeled to occur when locally the slope exceeds Φ_i = 40°. The failure plane is modeled to develop at Φ = 33°. Note that in the modeling herein, Φ is set equal to θ_{rm}; however these parameters do not necessarily have to be equal.

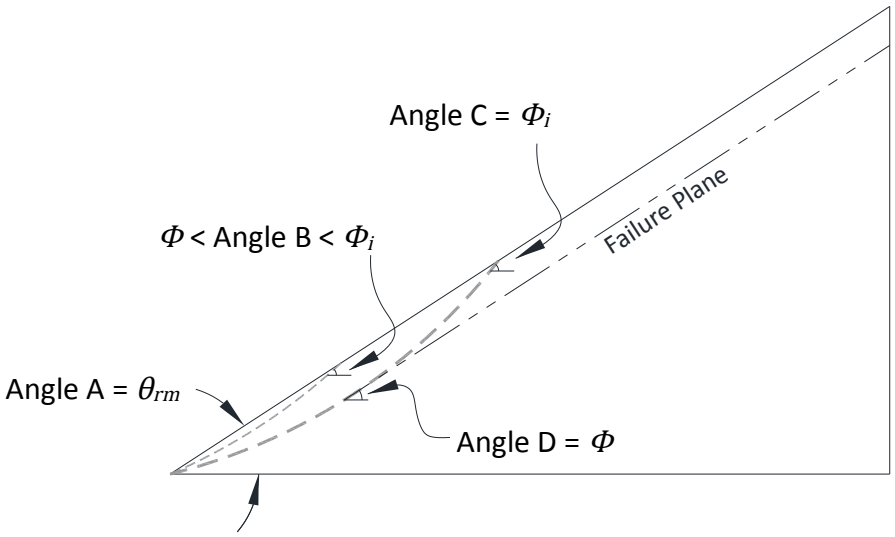

Figure 6: Schematic of Mass Failure concepts. Angle A is the initial condition at time t_0 with the surface at the mass angle of repose, θ_{rm} = 33°. The short-dashed line is the surface at time $t_1 > t_0$; the maximum angle B is greater than Φ, but less than Φ_i. The long-dashed line is the surface at time $t_2 > t_1$; the maximum angle C is just equal to Φ_i and so an avalanche is initiated; avalanching occurs along a failure plane (illustrated by the dashed line with long and short segments) at angle D equal to Φ.

3. Modeling Approach and Rationale

Cohesive sediment erosion formulations take the general form of Eq. (1) (Partheniades, 1965; Arulanandan et al., 1980):

$$\varepsilon = k_d(\tau_b - \tau_c)^a \tag{1}$$

where ε is the fluvial erosion rate; k_d is an empirically determined erodibility coefficient; τ_b is the boundary shear stress; τ_c is the critical boundary shear stress required to initiate motion of the bank material; and a is an empirical exponent generally found to be equal to 1. In the context of bank migration, ε can be expressed as $\Delta\xi/\Delta t$, where $\Delta\xi$ represents the lateral bank migration distance at the top of the layer in the direction normal to the channel centerline and t represents time. $\Delta\xi$ is measured at the top of the layer as a standard of reference to avoid ambiguous interpretations in cases where erosion only occurs over a portion of the bank. This is the form utilized by Motta et al (2012a) to provide a physical basis for fluvial erosion rates in the bank erosion submodel of RVR Meander-CONCEPTS.

Implicit in the formulation of Eq. (1) is the principle of sediment mass conservation; in the case of fine-grained cohesive sediment that is transported fully in suspension, the boundary experiences entrainment but no concurrent deposition. Therefore the entrainment rate dictates the boundary deformation. In non-cohesive material mobilized as bedload, a simple formulation similar to Eq. (1) is not possible because entrainment and deposition occur concurrently; boundary deformation must be found by coupling a bedload transport relation with the equation of sediment mass conservation. While Eq. (1) can be accurately applied to a point in the spatial domain for cohesive sediment, information on sediment transport from the adjacent areas is also required when evaluating boundary deformations in non-cohesive sediment. The 2D sediment mass conservation equation is expressed as follows:

$$\frac{\partial \eta}{\partial t} = -\frac{1}{(1-\lambda)}\left(\frac{\partial q_{s,s}}{\partial s} + \frac{\partial q_{s,n}}{\partial n}\right) \tag{2}$$

where η represents bed/bank elevation above an arbitrary datum; t is time; λ is porosity; $q_{s,s}$ is volumetric sediment transport rate per unit width along the streamwise coordinate; $q_{s,n}$ is volumetric sediment transport rate per unit width along the transverse (normal) coordinate; s is the spatial distance along the streamwise coordinate; n is the spatial distance along the transverse (normal) coordinate.

The goal of the current study is to determine if a simple form similar to Eq. (1) can represent in a gross sense the more complex physics embodied in a coupled 2D bedload transport relation with sediment mass conservation equation per Eq. (2). One potential approach would involve evaluating the results of a numerical model and forming correlations between the

hydrodynamic variables and the bank migration rates. For example, a morphodynamic model similar to that developed by Nagata et al (2000) or Jang and Shimizu (2005) could be evaluated over the short space and time scales practicable of such a model; those models link a 2D hydrodynamic submodel, bed evolution submodel, and bank evolution submodel incorporating 2D bedload transport and sediment mass conservation. However, implementing a more simplified model has greater potential to extract characteristic bank response to hydrodynamic variables. To meet that objective, the bank erosion model must be simplified to the extent possible without losing the essential physics; the quality of the model will be dictated by the assumptions.

The term $q_{s,s}$ in Eq. (2) can be determined from existing bedload formulations. The term $q_{s,n}$ is more complicated, and requires knowledge of the bank slope ω. In its simplest form it can be expressed as:

$$q_{s,n} = f(\tau^*, \tau^*_{c0}, \omega) \tag{3}$$

$$\tau^* = \frac{\tau_b}{\rho g R D_{50}} \tag{4}$$

where τ^* is the dimensionless Shields parameter; τ^*_{C0} is the critical value of τ^* that just initiates sediment motion on a flat bed; τ_b is the boundary shear stress; ρ is the water density; g is the gravitational acceleration constant; R is the submerged specific gravity of the sediment calculated as $(\rho_s - \rho)/\rho$; ρ_s is the sediment density; and D_{50} is the median diameter of the grain size distribution.

In evaluating potential simplications for Eq. (2), the $\partial q_{s,n}/\partial n$ term shall be considered first. One technique utilized in the past has been to integrate Eq. (2) over the n coordinate from the base of the bank to the top of the bank (e.g., Hasegawa, 1989; Parker et al, 2011). For example, integrating Eq. (2) over the eroding bank yields:

$$(1-\lambda)\int_{toe}^{tob}\left(\frac{\partial \eta}{\partial t}dn\right) = -\int_{toe}^{tob}\left(\frac{\partial q_{s,s}}{\partial s}dn\right) - \int_{toe}^{tob}\left(\frac{\partial q_{s,n}}{\partial n}dn\right) \tag{5}$$

where 'tob' represents the transverse coordinate associated with the top of bank; and 'toe' represents the transverse coordinate at the toe of the bank. The right-most integral pertaining to the $q_{s,n}$ terms yields $(q_{s,n}|_{\text{top}} - q_{s,n}|_{\text{toe}})$. If a similarity assumption is realistic, then all the variables in Eq. (3) are known and $(q_{s,n}|_{\text{top}} - q_{s,n}|_{\text{base}})$ can readily be calculated. With parallel bank retreat under a similarity function for the bank profile, the integral on the left hand side is also greatly simplified; see Hasegawa, 1989. The similarity assumption commonly utilized in the past is that of parallel bank retreat of a bank with uniform slope (e.g., Parker et al, 2011). A major premise of the current analysis is that a parallel bank retreat similarity assumption is not realistic under many circumstances. This will be demonstrated in the numerical modeling, but

such a premise is suggested on the basis of previous research. Past mechanistic studies of non-cohesive stream bank erosion have primarily focused on channel widening to an equilibrium condition (e.g., Parker, 1978; Pizzuto, 1990; Kovacs and Parker, 1994). Equilibrium bank profile form was demonstrated by Parker (1978) to exist when the bank adjusted its profile to generate vanishing transverse bedload $q_{s,n}$ (i.e., a static equilibrium). However, when a bank is actively migrating, a static equilibrium is by definition not obtained. At the interface of active bank transport, theoretically $q_{s,n}$ = 0, because the boundary shear stress at the interface is insufficient to mobilize material ($q_{s,s}$ = 0 and $q_{s,n}$ = 0); on the other hand, $q_{s,n}$ > 0 in the region of active transport. When the lower boundary of the bank domain is fixed, this suggests a continual reduction of slope toward zero transverse slope. This issue will be explored in greater detail in the numerical simulations.

Potential simplifications for the $\partial q_{s,s}/\partial s$ term in Eq. (2) shall now be considered. In the studies cited above regarding channel widening (Parker, 1978; Pizzuto, 1990; Kovacs and Parker, 1994), a straight channel was considered with uniform flow. Under such circumstances $\partial q_{s,s}/\partial s = 0$ and the term can therefore be dropped. The assumption of "locally uniform" conditions in the streamwise direction is also made in this analysis. This is partly necessary due to the generalization intended for this model (i.e., all possible spatial configurations associated with adding the streamwise spatial coordinate could not be analyzed in a general way); but some justification for this assumption for natural rivers was provided by Hasegawa (1989). In that study, an order of magnitude analysis was performed for each term in the sediment mass conservation equation, and it was found that for the range of values of the variables expected in a natural river the $\partial/\partial s$ terms were dominated by the $\partial/\partial n$ terms, and therefore the $\partial/\partial s$ terms could be reasonably neglected.

Therefore, the modeling approach considers locally uniform conditions in the streamwise direction that approximates straight channel flow. When considering a single cross-section, such a system can be readily expressed in standard Cartesian coordinates with x equivalent to s and y equivalent to n. Therefore Equation (1) can be rewritten:

$$\frac{\partial \eta}{\partial t} = -\frac{1}{(1-\lambda)}\left(\frac{\partial q_{s,y}}{\partial y}\right) \tag{6}$$

A bedload transport formulation is required for implementation in Eq. (6) that takes into account the large side slopes that may be observed on channel banks. Kovacs and Parker (1994) derived a formulation for equilibrium bedload transport that accounted for large side slopes; that relation is generalized to the case of slopes in both the streamwise and transverse directions, along with flow velocities and bed shear stresses that have both streamwise and transverse components. The formulation used herein is derived using the same principles as Kovacs and Parker (1994), but is simplified to the case of very small streamwise slope on the

order of typical longitudinal bed slopes present in alluvial low-land rivers. The full derivation is provided in Appendix A and yields the sediment trajectory deviation angle β with respect to flow velocity direction on the inclined surface. Under the simplifying assumption that the flow velocity is directed only in the streamwise direction, the derivation yields Equation (7). Illustration of the relevant geometry is provided in Figure 7.

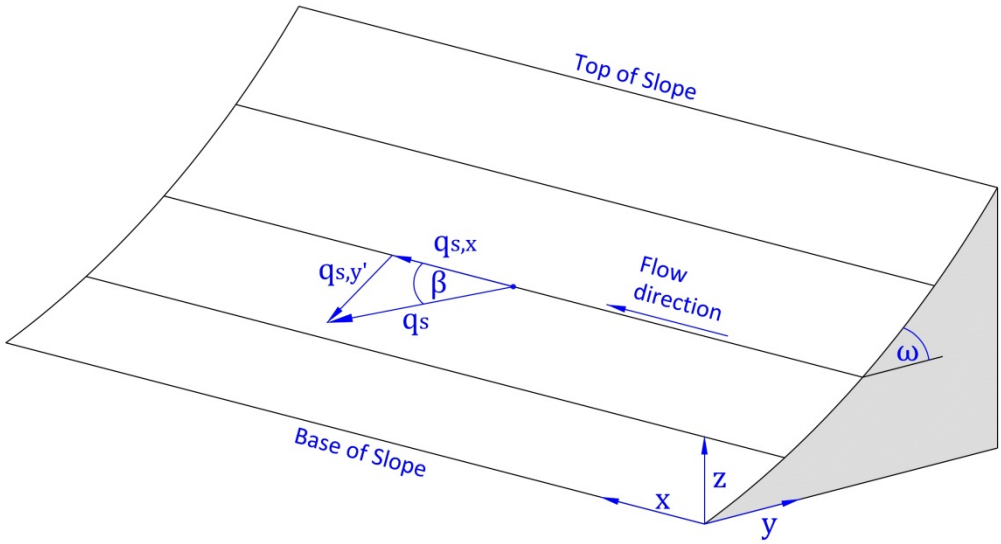

Figure 7: Definition Diagram for transverse bedload; isometric view. The y coordinate is perpendicular to the streamwise coordinate x on the plane with $z = 0$. The y' coordinate varies locally and is perpendicular to the streamwise coordinate on the inclined plane of the bank surface. The angle β and qs,y' both have negative values when directed as shown per the coordinate system used.

$$\frac{q_{s,y'}}{q_{s,x}} \equiv \tan\beta = -\frac{\left(\frac{\mu}{\mu_s}\right)^{1/2}\left[\frac{\cos\omega}{\left(1+\left(\tan\beta+\frac{1\tan\omega}{\mu\cos\beta}\right)^2\right)^{1/2}\cos\beta}\right]^{1/2}}{\mu}\sqrt{\frac{\tau^*_{c0}}{\tau^*}}\cdot\tan\omega \tag{7}$$

where $q_{s,x}$ is the bedload transport rate in the longitudinal direction; $q_{s,y'}$ is the bedload transport rate on the inclined surface perpendicular to the x-direction; β is the sediment trajectory deviation angle on the inclined surface; ω is the local transverse slope angle; μ is the dynamic friction coefficient, set equal to 0.5 (Engelund and Fredsoe, 1976); μ_s is the static friction coefficient, defined as follows:

$$\mu_s \equiv \tan\theta_{rp} \tag{8}$$

Because Eq. (7) is an implicit equation with β on the right-hand side, β must be solved iteratively. On geometric grounds, $q_{s,y'}$ can be converted to $q_{s,y}$ on the Cartesian coordinate system.

$$q_{s,y} = q_{s,y'}\cos\omega = q_{s,x}\tan\beta\cos\omega \tag{9}$$

The bedload formulation of Fernandez-Luque and vanBeek (1976) was obtained from experiments performed on high longitudinal slopes, and therefore that bedload formula is considered to best represent the physical conditions of the banks of the current model relative to other empirical formulas determined using experiments with flat beds:

$$q_{s,x}^{*} \equiv \frac{q_{s,x}}{\sqrt{gRD_{50}}D_{50}} = 5.7(\tau^{*} - \tau_{c}^{*})^{1.5} \tag{10}$$

where $q^{*}_{s.x}$ is the dimensionless bedload transport rate and τ^{*}_{c} is the Shields parameter for initiation of particle motion for the given slope condition. A particle is more readily mobilized on a slope because of the component of gravity acting on it in the downslope direction. Glover and Florey (1951) derived the slope factor K that modifies τ^{*}_{c0} for a particle located on a transverse slope and subject to a fluid drag force directed in the downstream direction:

$$\tau_{c}^{*} = K\tau_{c0}^{*} \tag{11}$$

$$K = \cos\omega\sqrt{1 - \frac{\tan^{2}\omega}{\tan^{2}\theta_{rp}}} = \sqrt{1 - \frac{\sin^{2}\omega}{\sin^{2}\theta_{rp}}} \tag{12}$$

where θ_{rp} is the particle angle of repose. The derivation for Eq. (12) assumes that the lift force can be neglected in the force balance. If the lift force is included, the parameter $\tau^{*}_{c}/\tau^{*}_{c,0}$ needs to be solved as a quadratic polynomial (Garcia, 2008). Equations 6 through 12 are the equations required in the numerical model.

4. Numerical Model

The numerical model is based on sediment mass conservation Eq. (6), which considers only the transverse and vertical coordinates. By substituting Eq. (9) through (12) into Eq. (6), it can be expressed as:

$$\frac{\partial \eta}{\partial t} = -\frac{1}{(1-\lambda)}\frac{\partial}{\partial y}\left[\tan\beta \cos\omega \, 5.7\sqrt{gRD_{50}}D_{50}\left(\tau^*(y) - \tau^*_{c0}\sqrt{1-\frac{\sin^2\omega}{\sin^2\theta_p}}\right)^{1.5}\right] \quad (13)$$

The τ^* versus y function represents the boundary shear stress distribution, which can be expressed with varying degrees of complexity. Lundgren and Jonsson (1964) provide a number of boundary shear stress distribution formulations that range from a constant cross-sectional average value at the simple end of the spectrum through a formulation that takes into account logarithmic velocity profiles normal to the boundary and lateral turbulent diffusion of momentum at the complex end of the spectrum. The simplest form that is reasonably realistic is referred to as the vertical depth method, in which τ^* is linear with the local flow depth:

$$\tau^*(y) = \tau^*_{base} \cdot \frac{h-\eta(y)}{h-\eta_{base}} \qquad \text{for } h > \eta_{base} \quad (14)$$

where h is the flow stage relative to the same vertical datum as η, and h is allowed to vary in time based on a hydrograph. η_{base} is the value of η at the base of the bank; τ^*_{base} is the value of τ^* at the base of the bank. It should be noted that although a simple linear formulation for the shear stress distribution has been selected, a more complex function could also be implemented in the model. A diagram illustrating some important variables and parameters is included as Figure 8.

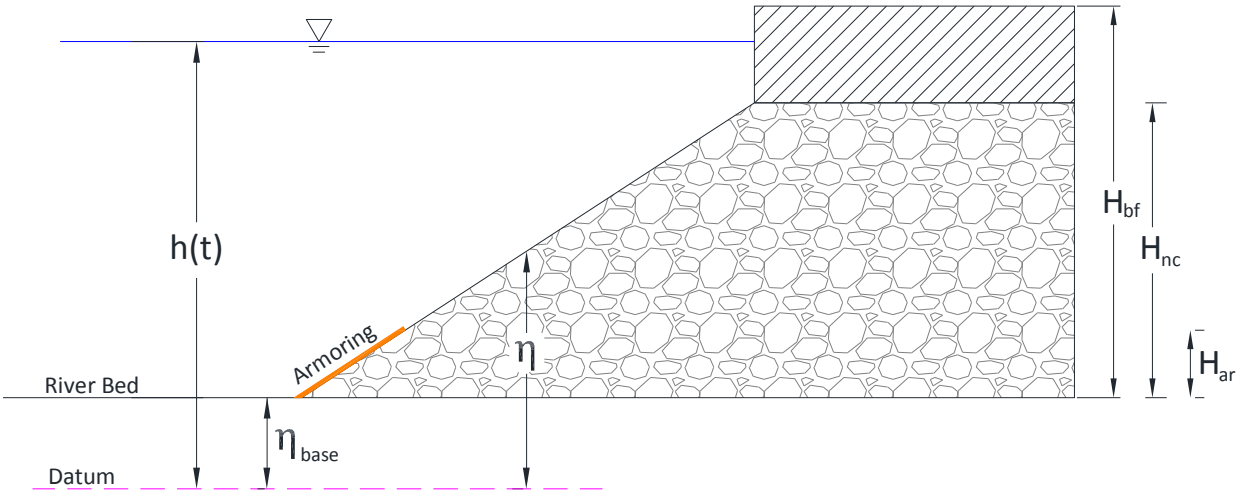

Figure 8: Cross section of modeled bank

In the above diagram H_{bf} represents the bankfull depth, H_{nc} represents the depth of the non-cohesive layer, and H_{ar} represents the depth of the basal armoring. The model assumes that all the non-cohesive bank material has uniform grain size and is unstructured (loosely packed). The numerical model evolves the bed only over the non-cohesive portion of the bank; this assumes that the upper cohesive layer migrates at the same rate at which the top of the non-cohesive layer migrates. This represents the condition where mass failures occur in the upper layer due to undercutting associated with the lower layer. Mass failures of the cohesive layer are not explicitly modeled, nor does the model account for their dynamic influence on basal armoring due to cohesive slump blocks.

To evaluate a hydrograph with h that varies with t, it is convenient to express τ^*_{base} as a function of (h - η_{base}). However, depending on the position in a bend, some portions of the bank will experience significantly higher values of τ^*_{base} than others, even though (h - η_{base}) may be equal. The relation between τ^*_{base} and (h - η_{base}) is not known *a priori*, as the value will ultimately be based on the output from a hydrodynamic submodel; so a range of values need to be evaluated. A realistic reference relationship for τ^*_{base} can be established as a function of reach-scale average channel variables. A momentum balance for a uniform wide, shallow channel in which the downstream gravitational force balances the frictional resistance force (i.e., normal depth) yields the following expression for the reference relationship:

$$\tau^*_{ref} = \frac{(h-\eta_{base})S_0}{RD_{50}} \tag{15}$$

$$\tau^*_{base} = \chi\tau^*_{ref} \tag{16}$$

where S_0 is the average longitudinal channel bottom slope; τ^*_{ref} is the reference value of τ^*_{base}; χ parameterizes the physical condition that the high-velocity core of the flow may be close or far from the bank, depending on the 2D channel plan form and the discharge. An important assumption, discussed in detail later, is that χ remains constant during the bank erosion simulations. χ should vary from about 0.5 to 2.5 between simulations to characterize the full range of shear stresses that an eroding bank may experience. χ will ultimately be determined by a separate hydrodynamic submodel. Figure 9 further illustrates the meaning of the parameter χ, as it is very important in later development of the bank erosion submodel.

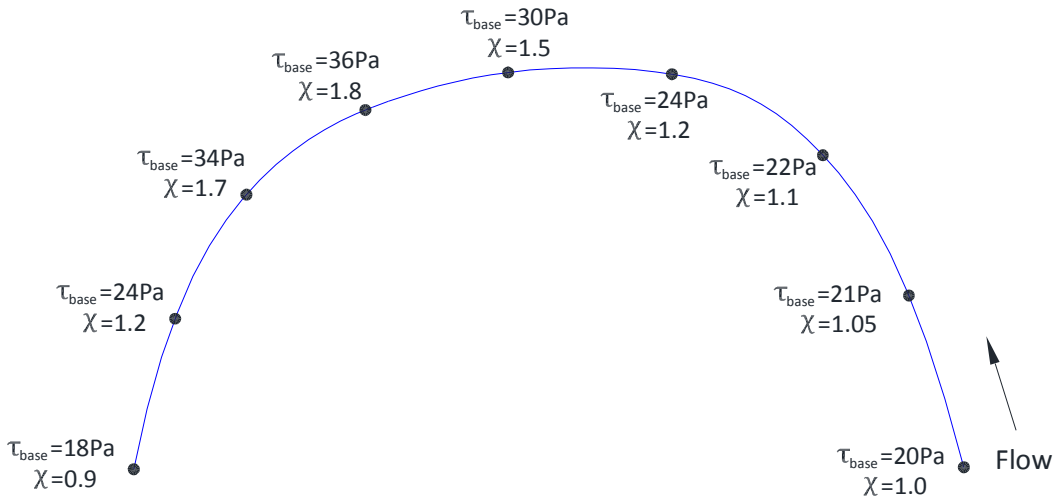

Figure 9: Illustration of the parameter χ along the right bank of an example meander bend. The hydrodynamic submodel yields the τ_{base} shown at each computational node and an average depth of approximately 3 meters. Using the mean channel variables, τ_{ref} is calculated as 20 Pa. The parameter χ is calculated at each node according to Eq. (16). τ_{base} and τ_{ref} are the dimensional equivalents of τ^*_{base} and τ^*_{ref} per Eq. (4). Note that bed scour as a function of curvature is also calculated in a hydrodynamic submodel; however, the method of the numerical simulations assumes that η_{base} is a constant.

Substituting Eq. (15) and (16) into Eq. (14) yields:

$$\tau^*(y) = \chi \frac{(h-\eta(y))S_0}{RD_{50}} \tag{17}$$

Substituting Eq. (17) and removing constants from the derivative term, Eq. (13) can be expressed as:

$$\frac{\partial \eta}{\partial t} = -\frac{5.7\sqrt{gRD_{50}}D_{50}}{(1-\lambda)} \frac{\partial}{\partial y}\left[\tan\beta \cos\omega \left(\chi \frac{(h-\eta)S_0}{RD_{50}} - \tau^*_{c,0}\sqrt{1-\frac{\sin^2\omega}{\sin^2\theta_p}}\right)^{1.5}\right] \tag{18}$$

Non-dimensionalization of the equations allows the results to be generalized across different scales. The following non-dimensional terms are introduced:

$$\eta^* = \frac{(\eta-\eta_{base})}{H_{bf}} \tag{19a}$$

$$h^* = \frac{(h-\eta_{base})}{H_{bf}} \tag{19b}$$

$$y^* = \frac{y}{H_{bf}} \tag{19c}$$

$$t^* = \frac{t}{T_{hyd}} \tag{19d}$$

where η^* is dimensionless bank elevation; h^* is dimensionless flow stage; y^* is dimensionless transverse coordinate; t^* is dimensionless time; H_{bf} is the bankfull depth; T_{hyd} is the duration of the hydrograph. When the assumption is made that $\partial \eta_{base}/\partial t = 0$ (this important assumption is discussed at the end of this section), the dimensionless form of Eq. (18) can then be expressed as:

$$\frac{\partial \eta^*}{\partial t^*} = -C_1 \frac{\partial}{\partial y^*}\left[\tan\beta \cos\omega \left(C_2(h^* - \eta^*) - \tau^*_{c0}\sqrt{1 - \frac{\sin^2\omega}{\sin^2\theta_{rp}}}\right)^{1.5}\right] \tag{20}$$

where C_1 and C_2 are dimensionless parameters:

$$C_1 = \frac{T_{hyd} 5.7\sqrt{gRD_{50}} D_{50}}{{H_{bf}}^2 (1-\lambda)} \tag{21a}$$

$$C_2 = \tau^*_{base,bf} = \chi \frac{H_{bf} S_0}{RD_{50}} \tag{21b}$$

The numerical model discretizes Eq. (20). The bed is evolved through time using an explicit, finite difference approach. The local bed slope $\tan\omega$ at numerical node i is calculated as a central difference using η^* values at nodes $i+1$ and i-1:

$$\tan\omega = \frac{(\eta^*_{i+1} - \eta^*_{i-1})}{2\Delta y^*} \tag{22}$$

The term $\tan\beta$ is solved iteratively per Eq. (7) using a bisection scheme. The term $\Delta[\tan\beta \cos\omega (C_2(h^*\text{-}\eta^*)\text{-}K\tau^*_{c,0})^{1.5}]$ is calculated according to a central difference method using values of the term in brackets calculated at nodes $i+1$ and i-1:

$$\gamma_i = \left[\tan\beta_i \cos\omega_i \left(C_2\left(h^*_i - \eta^*_i\right) - \tau^*_{c,0}\sqrt{1 - \frac{\sin^2\omega_i}{\sin^2\theta_{rp}}}\right)^{1.5}\right] \tag{23}$$

$$\frac{\Delta\left[\tan\beta \cos\omega\left(C_2(h^* - \eta^*) - \tau^*_{c,0}\sqrt{1 - \frac{\sin^2\omega}{\sin^2\theta_p}}\right)^{1.5}\right]}{\Delta y^*} = \frac{\gamma_{i+1} - \gamma_{i-1}}{2\Delta y^*} \tag{24}$$

Mass failure avalanches are specified using a heuristic scheme similar to that of Hasegawa (1981) and Pizzuto (1990). When the local slope angle ω exceeds the angle of initial yield Φi, then the avalanche algorithm is initiated which causes bank material located above the failure plane illustrated in Fig. 6 to be mobilized and deposited downslope, coming to rest at the mass

angle of repose θ_{rm}. This yields discrete avalanche events, which are calculated between time steps; it is assumed the avalanche occurs instantaneously and does not otherwise influence the calculated bedload processes at the previous or following time steps. Shallow avalanching of the non-cohesive layer does not involve the cohesive upper layer. The avalanche algorithm is described in detail in Appendix B.

The boundary conditions of the model represent important assumptions. At the lower boundary, the most simple realistic condition is that the toe of the bank is a fixed boundary such that $\partial \eta_{base}/\partial t = 0$ and $\partial y_{base}/\partial t$ = 0. This is a flux boundary condition where the entire transverse sediment load at the lowest computational node is passed out of the modeled domain. In reality, material may accumulate or scour in the bed region at the base of the slope, and such a condition would have significant effect on the bank migration rate per the basic principles of basal endpoint control (Thorne, 1982). The chosen boundary condition represents several realistic natural situations: (a) the river bed is supply-limited with respect to the sediment size input from the bank region, and the river then transports that material without undergoing aggradation or degradation at the toe; (b) the longitudinal gradient in bed sediment transport rate is tending to scour the bed at the toe, but the bank material input offsets the scouring tendency. The latter corresponds to the state of "unimpeded removal" with respect to basal endpoint control (Thorne, 1982). Conditions certainly exist where such a boundary condition neglects the dominant control on bank migration. In such circumstances, a more complete morphodynamic model incorporating both bed and bank regions would need to be implemented rather than the 1D transverse coordinate approach used in this analysis; the intent of the current analysis is to isolate bank processes. The boundary condition at the top of the non-cohesive layer is that $q_{s,n}$ = 0; in other words, the cohesive layer is not providing bedload-sized material to the non-cohesive layer.

5. Characteristic Forms of the Eroding Bank Profiles

The numerical model results reveal three characteristic forms of the bank profiles; the dominant control on the form is the vertical position on the bank where (τ^*/τ^*_c) = 1. The three characteristic forms do not represent abrupt phase changes occurring at threshold values; the transition between types is on a gradation. The three types can actually all occur at different times within the same hydrograph, as the vertical position on the bank where (τ^*/τ^*_c) = 1 changes during the hydrograph. The characteristic forms are illustrated in examples using a constant flow stage h^* and therefore a constant τ^*_{base} during each simulation; the initial value of (τ^*/τ^*_c) = 3.0 at the base of the bank at initial time is used in each simulation; T_{hyd} in each example is 8 hours. The simulations utilize the fixed lower boundary condition, $\partial\eta_{base}/\partial t = 0$ and $\partial y_{base}/\partial t$ = 0. The parameters of the model for the simulations are as follows: θ_{rm} = 33°; θ_{rp} = 50°; Φ = 33°; Φ_i = 40°; D_{50} = 15 mm; τ^*_{C0} = 0.045, which applies to the gravel material selected for the modeling; R = 1.65; μ = 0.5; $\mu_s \equiv \tan\theta_p$ = 1.19; λ = 0.35; H_{bf} = 4 m. The parameters for D_{50} and H_{bf} were chosen to be representative of the Mackinaw River field site shown in Figures 2 through 5. A reference initial condition in the modeling is a constant slope situated at the mass angle of repose θ_{rm}, as would exist following a deep basal scour in the bed region followed by mass avalanche.

Type 1: Concave base and convex upper slope

This type of bank deformation occurs when (τ^*/τ^*_c) at the top of the non-cohesive layer is approximately 1.5 or greater; in other words, the vertical position where $(\tau^*/\tau^*_c) = 1$ is higher than the top of the non-cohesive layer. Because τ^* goes to 0 where the bank elevation equals the water surface elevation, this conditions persists only when the entire non-cohesive layer is submerged. Such a condition would be most prevalent when the non-cohesive sediment layer does not extend far up the bank; in other words, when H_{nc} / H_{bf} is small (see Fig. 8). The migration rate as measured at the top of the non-cohesive layer is largely dictated by processes occurring in the convex part of the profile. No shallow avalanching occurs in the non-cohesive layer, as the bank continually reduces its slope over time.

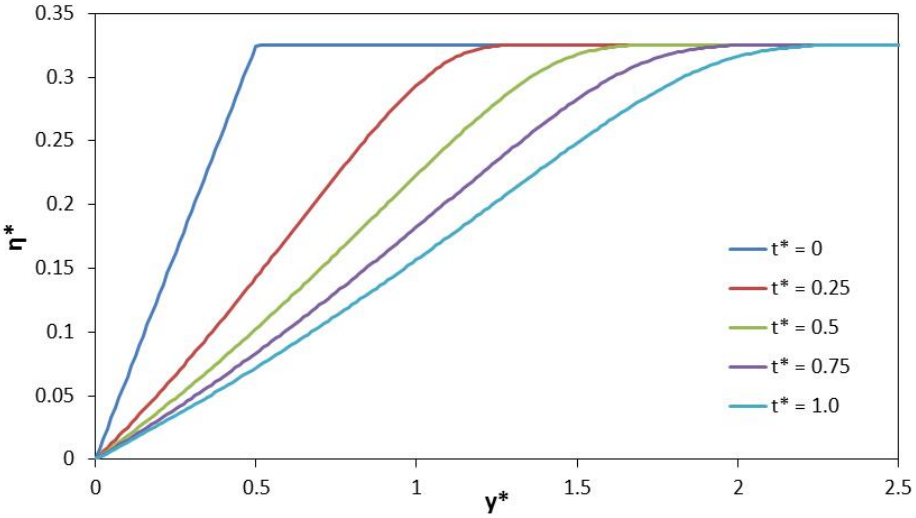

Figure 10: Type 1 non-cohesive bank erosion. For this simulation, H_{bf} = 4 m; H_{nc} = 1.3 m; T_{hyd} = 8 hrs; h = 3 m (ie, the flow is at 3/4 bankfull depth); (τ^*/τ^*_c) = 3.0 initially at the base; and (τ^*/τ^*_c) = 1.7 initially at the top of the non-cohesive layer. Total migration at the top of the non-cohesive layer in this simulation is 6.90 m. The visualization only extends to the top of the non-cohesive layer.

It is evident from Fig. 10 that the rate of bank deformation decreases substantially as the slope becomes less steep.

Type 2: Concave throughout profile

This type of bank deformation occurs when the vertical position where $(\tau^*/\tau^*_c) = 1$ is near the top of the non-cohesive layer. When (τ^*/τ^*_c) at the top of the non-cohesive layer is between 1.0 and approximately 1.5, a convex part of the upper profile results, but it is of limited extent. When the location where $(\tau^*/\tau^*_c) = 1$ drops below the top of the non-cohesive layer, then the slope can steepen beyond Φ_i just below the $(\tau^*/\tau^*_c) = 1$ interface, resulting in avalanching that originates high up the bank. The mass of material that is avalanched is generally not sufficient to fully infill the concave form below, so that the concave lower part of the profile is maintained. The Type 2 deformation would be the predominant form during high flows when the non-cohesive layer extends well up the bank.

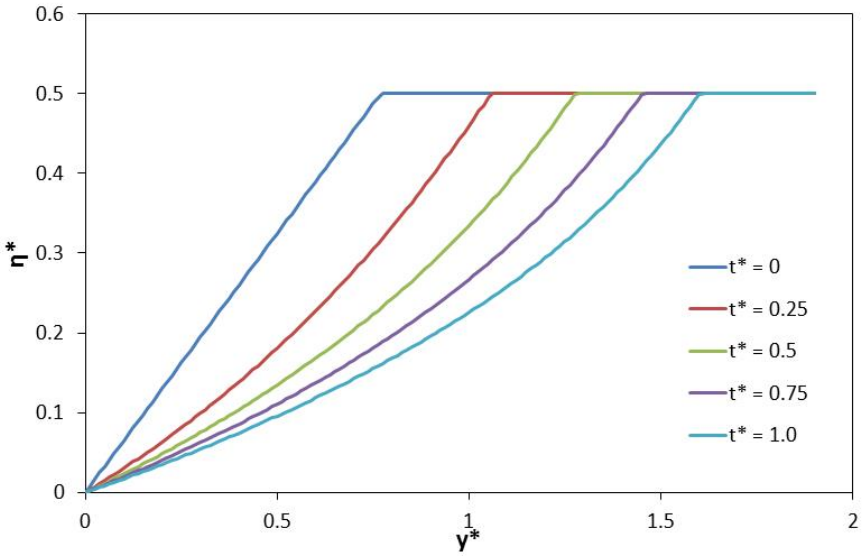

Figure 11: Type 2 non-cohesive bank erosion. For this simulation, H_{bf} = 4 m; H_{nc} = 2.0 m; T_{hyd} = 8 hrs; h = 3 m; (τ^*/τ^*_c) = 3.0 initially at the base; and (τ^*/τ^*_c) = 1.0 initially at the top of the non-cohesive layer. Total migration at the top of the non-cohesive layer in this simulation is 3.35 m. The visualization only extends to the top of the non-cohesive layer.

The bank evolution shown in Fig. 11 was simulated using the same parameters as that shown in Fig. 10, with the only difference being H_{nc}. The greater depth of the non-cohesive layer mitigates the magnitude of bank retreat. This is readily explained when considering the region of the bank with vertical position of η^* = 0.325; under the previous simulation shown in Fig. 10, $\partial q_{s,y}/\partial y$ at that position was very high, because the $q_{s,y}$ input at the top of the non-cohesive layer was 0; whereas in Fig. 11, the upslope region provides transverse bedload to that position and so $\partial q_{s,y}/\partial y$ has a smaller value. The reduction of the slope through time also leads to decelerating bank retreat as in Figure 10. No avalanches occurred in the simulation illustrated in Figure 11.

Type 3: Semi-Parallel retreat; basal deformation followed by avalanching

This type of bank deformation occurs when the vertical position where (τ^*/τ^*_c) = 1 is well below the top of the non-cohesive layer. Over-steepening occurs in the region just downslope from the interface between mobile and immobile non-cohesive bank material. Avalanching mobilizes material all the way to the top of the non-cohesive material when the upper bank material is at steep angles; if the bank started out with a lower angle, the avalanche would only extend part of the way up the slope until the failure plane (Fig. 6) intersected with the existing ground surface. Deformation near the base of the bank would have the effect of steepening the slope in the latter circumstance. This type of deformation would predominate during low and moderate flow stages that generated sufficient boundary shear stress to mobilize lower bank material, or where the non-cohesive material extended nearly to the bank-full level or higher (e.g., when the bank is eroding into a terrace, which is an abandoned floodplain formed in a previous geomorphic setting).

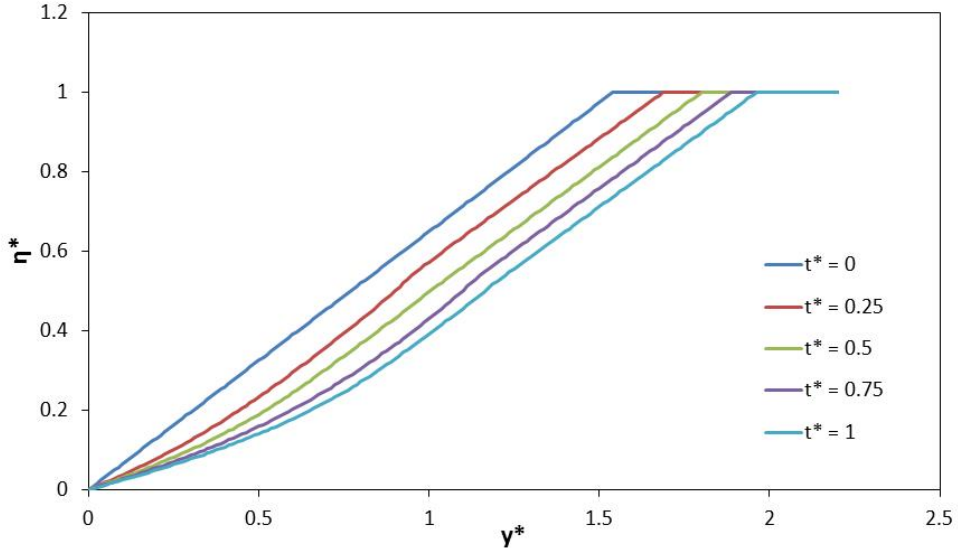

Figure 12: Type 3 non-cohesive bank erosion. For this simulation, H_{bf} = 4 m; H_{nc} = 4.0 m; T_{hyd} = 8 hrs; h = 3 m; (τ^*/τ^*_c) = 3.0 initially at the base; and (τ^*/τ^*_c) = 1 at η^* = 0.5. Total migration at the top of the non-cohesive layer in this simulation is 1.65 m. The visualization includes the entire height of the bank.

In the above simulation, 33 discrete shallow avalanches occurred during the simulation that included 9,600 time steps. It is evident that the rate of retreat decelerates with time as the base becomes less steep. It should be noted that the region from η*=0.75 to η*=1.0 in this simulation is above the river water level, and therefore the non-cohesive bank material in that region is likely unsaturated and experiences an effective cohesion due to capillary forces. The presence of effective cohesion would cause the failure plane angle to steepen; the modified failure plane angle in the subaerial region has been considered in past modeling efforts such as Nagata et al (2000) and Nasermoaddeli and Pasche (2010); herein for simplicity it is assumed that the failure plane angle is constant to the top of the non-cohesive material.

6. Influence of Basal Armoring

If the lower part of the bank is rendered immobile due to armoring (e.g., cohesive slump blocks, basal non-cohesive material strengthened by silt and clay deposits), this can feed back on the bank retreat as measured at the top of the non-cohesive layer; the magnitude of the feedback depends on which of the three forms of bank deformation is predominant, how much of the lower bank is armored, and how long the armoring persists. The effect of basal armoring is obvious in the case where the armoring covers the entire portion of the bank having $(\tau^*/\tau^*_c) > 1$ in the unarmored state; in such case, the basal armoring would fully arrest bank migration until the armoring was eliminated. It should be noted that when armoring reduces the input of sediment from the bank region to the bed region, this can lead to bed scour, perhaps triggering mass failures originating at the base of the slope due to destabilization of the base (Thorne, 1982). Because the current modeling domain only extends to the toe of the bank and does not include bed processes, that dynamic effect of armoring is not quantified. In the case where armoring does not cover the entire portion of the bank having $(\tau^*/\tau^*_c) > 1$, the effect on bank retreat is not as obvious and will be illustrated with examples.

To demonstrate the feedback associated with basal armoring on bank retreat above the armored layer, the same simulations are run as in Figures 10 through 12; but the base is armored from $\eta^* = 0$ up to $\eta^* = 0.175$. To model the condition of basal armoring, it is assumed that the armored region is immobile and therefore acts to bypass transverse bedload delivered from upslope without undergoing deformation in the armored region.

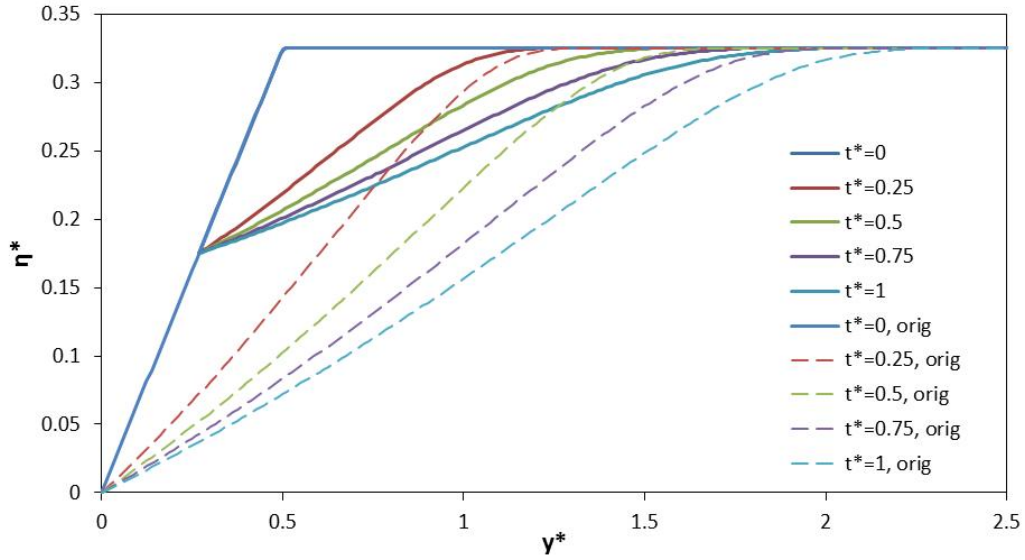

Figure 13: Type 1 non-cohesive bank erosion with basal armoring. The simulation parameters are identical to that of Fig. 10; the curves from Fig. 10 are shown as dashed lines for reference. Total migration at the top of the non-cohesive layer in this simulation is 5.90 m, which is 85.5% of the total from the original case with no basal armoring. The visualization only extends to the top of the non-cohesive layer.

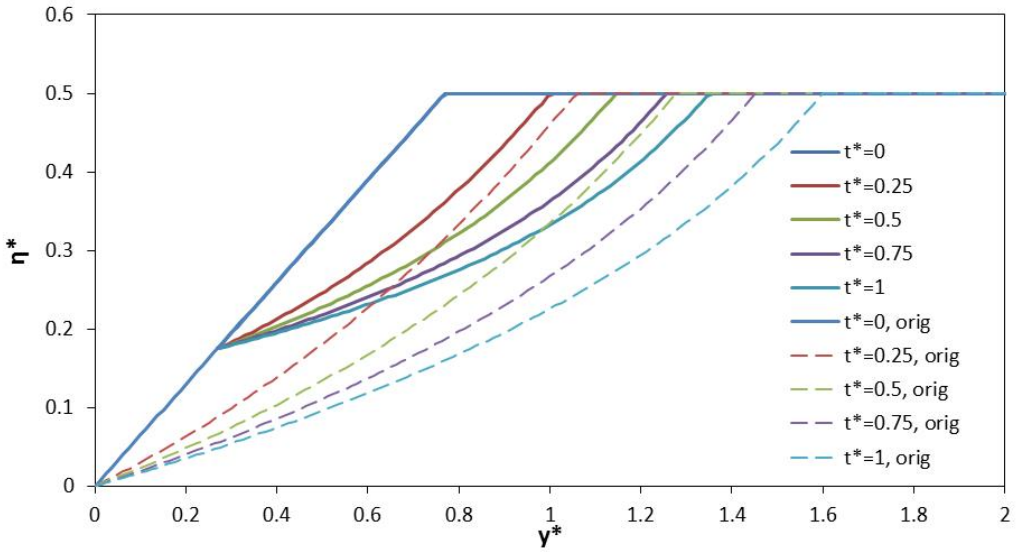

Figure 14: Type 2 non-cohesive bank erosion with basal armoring. The simulation parameters are identical to that of Fig. 11; the curves from Fig. 11 are shown as dashed lines for reference. Total migration at the top of the non-cohesive layer in this simulation is 2.30 m, which is 68.7% of the total from the original case with no basal armoring. The visualization only extends to the top of the non-cohesive layer.

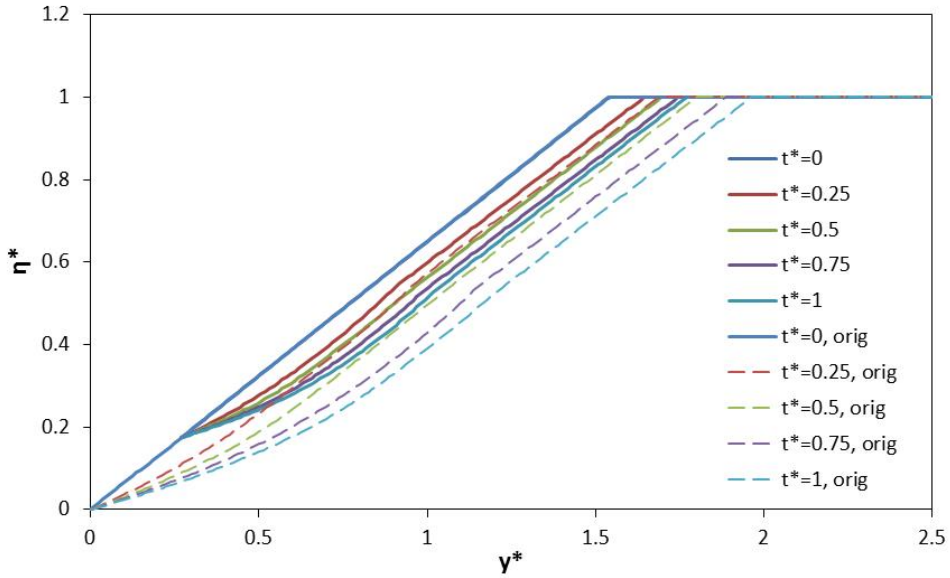

Figure 15: Type 3 non-cohesive bank erosion with basal armoring. The simulation parameters are identical to that of Fig. 12; the curves from Fig. 12 are shown as dashed lines for reference. Total migration at the top of the non-cohesive layer in this simulation is 0.90 m, which is 54.5% of the total from the original case with no basal armoring.

In the case of Type 1 bank deformation shown in Fig. 13, even though the armoring covers over half of the non-cohesive layer that is mobile in the unarmored state, the armoring has minimal effect because the retreat of the top of the non-cohesive layer is largely dictated by the convex part of the bank profile. However, it should be noted that in the example shown, over 2/3 of

the bank height is comprised of cohesive upper layer material (from η^* = 0.325 to η^* = 1.0). The rapid deformation of the lower non-cohesive layer would be expected to result in mass failure of the upper cohesive layer; the first large volume failure would likely fully armor the lower bank, thus arresting the migration until the armoring material is eroded. Dynamic basal armoring that is a function of non-cohesive layer retreat is not implemented in the current model, although it could be implemented in a more sophisticated model using the same general approach.

In the case of Type 2 and Type 3 bank deformation, the basal armoring covers less than half of the non-cohesive layer that is mobile in the absence of armoring; but the feedback on the retreat measured at the top of the non-cohesive layer is more substantial, reducing the total migration to nearly half in the Type 3 case. If the basal armoring covered a greater portion of the mobile region, it can be readily demonstrated that the migration can be reduced by over an order of magnitude.

The shape of the profiles shown in Fig. 13 through 15, with an immobile basal region forming a bench and a deforming bank above the basal region, can be observed in the field. Fig. 16 below shows a migrating bank just downstream of the field site shown in Fig. 2 where the lower bank is protected through bendway weirs that extend vertically to less than the full height of the non-cohesive lower layer. The lower bank protection has mitigated, but not fully arrested bank retreat. It is important to note that mitigation of the bank migration rate in this situation is due not only to protection of the base, but also the alteration of the flow field and boundary shear stress due to the weirs.

Figure 16: Bank erosion with lower bank protection at Mackinaw River

7. Ultimate Linkage to a Hydrodynamic Submodel

The bank erosion submodel is best developed keeping in mind how it will be linked to a hydrodynamic submodel; the outputs from the hydrodynamic submodel will be fed into the bank erosion submodel to determine bank migration distance. Therefore, understanding the outputs and limitations of the hydrodynamic model are key considerations in developing the bank erosion submodel.

Due to the large time scales simulated in a model such as RVR Meander-CONCEPTS, simulating instantaneous discharge within a hydrograph is not practicable. A single model discharge (Q_{mod}) that best characterizes bank erosion with a coupled intermittency of discharge (I_{mod}) is the most computationally efficient approach; hereafter, the subscript 'mod' used for other variables also indicates a modeled value. The appropriate values for Q_{mod} and I_{mod} can ideally be determined using the following steps:

a. Utilize a flow duration curve discretized into N discharge ranges;
b. Model $(\Delta\xi/\Delta t)_i$ associated with each discharge range, where $\Delta\xi$ represents the migration distance at the top of the non-cohesive layer, and i represents an individual bin of the discretized flow duration curve;
c. Integrate $(\Delta\xi/\Delta t)_i$ x Δp_i for the entire range i = 1 to N, where Δp_i is the probability of occurrence of the discharge range, as determined from the flow duration curve; this integration yields a value $(\Delta\xi/\Delta t)_{net}$;
d. Select Q_{mod} and I_{mod} such that $(\Delta\xi/\Delta t)_{mod}$ x I_{mod} is equal to the $(\Delta\xi/\Delta t)_{net}$ value determined through the integration above; (note that a multitude of combinations of Q_{mod} and I_{mod} satisfy this criterion).

The above treatment follows the logic of a "model discharge" approach used in sediment transport applications.

The ideal approach described above could be readily implemented for bank erosion if the bank profiles were realistically represented with a similarity function. However, although the concave shape is fairly general, the transverse slope does not tend to a characteristic value; high stage events tend to cause a decrease in net slope and low stage events tend to increase the net slope. This causes complications in determining values of $(\Delta\xi/\Delta t)_i$ specified in Step [b], due to the strong dependence of $(\Delta\xi/\Delta t)_i$ on the prior erosional history. Even in a single hydrograph whose rising phase and falling phase are perfectly symmetric, different deformation rates are experienced on the rising phase and the falling phase. This suggests that $(\Delta\xi/\Delta t)_i$ must be determined at least partly in a statistical manner, which takes into account the many possible configurations of the bank profile.

The goal of the bank erosion submodel is to develop a simplified equation that represents in a gross sense the bank migration rates as a function of hydrodynamic variables similar to Eq. (1): $\Delta\xi/\Delta t = k_d(\tau_b - \tau_c)^a$. The hydrodynamic model will output a value of τ_{base} associated with Q_{mod} as shown in Fig. 9, and so the appropriate value of τ_b in the formulation is τ_{base}. Two different approaches were considered to develop a function of the above form: (i) fit a function of the form $(\Delta\xi/\Delta t)_i$ versus $(\tau^*_{\text{base}} - \tau^*_{\text{c}})_i$ per Eq. (1); (ii) fit a simplified function of $(\Delta\xi/\Delta t)_{net}$ versus χ. The two approaches are discussed below, along with the rationale for selecting Approach (ii).

Approach (i): This approach involves modeling a representative flow rate for each bin on the flow duration curve and determining the associated $(\Delta\xi/\Delta t)_i$ and $(\tau^*_{base} - \tau^*_c)_i$, which comprises a point on the plot. For each representative flow rate, a range of values of χ must be evaluated. Each evaluation yields a separate point on the plot. A curve is fit to the plotted points.

For example, let us use the Mackinaw River variables described at the end of Section 4. We shall evaluate an arbitrary bin i = 5 on the flow duration curve, which is associated with a range of discharge Q between 5500 and 6500 cfs. Bank deformation is modeled for a representative Q = 6000 cfs. From a stage-discharge relationship for the reach, ($h - \eta_{base}$) is found to be 3.0 m for this discharge. From Eq. (13), τ^*_{ref} is found to be 0.085. For the evaluation of χ = 1, τ^*_{base} = 0.085 from Eq. (14). The value $(\tau^*_{base} - \tau^*_c)_i$ is then calculated as 0.040. A suite of initial bank profiles is modeled using these flow variables and $(\Delta\xi/\Delta t)_i$ is found to have an average value of 0.011 m/hr. This value of $(\Delta\xi/\Delta t)_i$ = 0.011 m/hr associated with $(\tau^*_{base} - \tau^*_c)_i$ =0.085 is plotted as a point. The process would be repeated in this discharge bin for the full range of χ to be evaluated; and it would then be repeated for all bins on the flow duration curve to develop the plot of $(\Delta\xi/\Delta t)_i$ versus $(\tau^*_{base} - \tau^*_c)_i$.

A complication arises in this approach. In the Mackinaw River example, we find that for discharge bin i = 2 associated with Q between 2500 and 3500, the stage-discharge relationship yields ($h - \eta_{base}$) = 2.0 m for the representative Q = 3000 cfs. When evaluating χ = 1.5, the value of $(\tau^*_{base} - \tau^*_c)_i$ is found to be 0.040, which is the same as for the bin i = 5 example described above. However, the erosion rates are considerably different, because the type of erosion shifted from Type 2 deformation for bin i = 5 to Type 3 deformation for bin i = 2. This suggests that $(\tau^*_{base} - \tau^*_c)_i$ is not the best choice of independent variable.

Let us evaluate the proposed independent variable more closely. The independent variable $(\tau^*_{base} - \tau^*_c)_i$ can also be written: $[\chi(h-\eta_{base})S_0/(RD_{50}) - \tau^*_c)_i$. Numerous combinations of $\chi(h - \eta_{base})$ can yield the same τ^*_{base}, but the erosion rate can be

different in each case. Because of this issue, the Eq. (1) form: $\Delta\xi/\Delta t = k_d(\tau_b - \tau_c)^a$ does not strictly hold; an extra independent variable is necessary. A possible alternative with multiple independent variables is of the form: $\Delta\xi/\Delta t = k_d\chi^a(h - \eta_{base})^b$. Rather than pursuing this course, a simpler approach was found to be more appropriate.

Approach (ii): The second approach yields a more straight-forward curve-fitting procedure. Rather than plotting $(\Delta\xi/\Delta t)_i$ versus several independent variables, the dependent variable is selected to be $(\Delta\xi/\Delta t)_{net}$; recall that $(\Delta\xi/\Delta t)_{net}$ is the integration of $(\Delta\xi/\Delta t)_i$ with Δp_i over all bins on the flow duration curve. χ is fixed during simulations over the entire range of bins to yield a point on the curve of $(\Delta\xi/\Delta t)_{net}$ versus χ. In such an approach, rather than treating χ and ($h - \eta_{base}$) independently as would be necessary in Approach (i), each evaluation of χ incorporates the full range of ($h - \eta_{base}$). The implications of using the fixed χ assumption at a single bank cross-section over a wide range of flows that would occur over a long period of time are discussed at the end of this section.

In addition to the benefit of a more straight-forward curve-fitting procedure, a second benefit of Approach (ii) becomes apparent when selecting Q_{mod} and I_{mod} to use in the hydrodynamic submodel. It is no longer necessary to determine I_{mod}, because $(\Delta\xi/\Delta t)_{net}$ incorporates the intermittency of the flow (as it is the result of integration with Δp_i). Therefore, selection of the appropriate Q_{mod} is the only remaining consideration; the exact value chosen serves only to determine the specific distribution of χ throughout the modeled domain. However, this is not arbitrary, as the choice of Q_{mod} should clearly be based on the discharge that is responsible for the most erosion over long periods of time, as this is the most relevant distribution of χ. An effective discharge approach is proposed; this has long been used in geomorphology to determine which flow rates transport the most sediment (Schaffernak, 1916; Wolman and Miller, 1960). The effective discharge is discussed in detail in §8.

Approach (ii) is chosen for the linkage between the hydrodynamic submodel and the bank erosion submodel due primarily to the advantage of simplicity. Numerous assumptions are inherent in the chosen Approach (ii) and these are discussed as follows.

The first assumption of the chosen approach is that for each simulation, χ remains constant over all the flow stages in all the hydrographs modeled. In reality, the locus of high velocity and high boundary shear stress may shift as stage changes; in other words, at a single location, the value of χ may vary over a single hydrograph and over multiple hydrographs. Variation in χ cannot be accounted for in a general way as it depends on the specifics of the plan-form geometry, cross-sectional shape, and the specific range of flows considered.

The second assumption involved in developing a bank erosion submodel independent of a hydrodynamic submodel pertains to the boundary shear stress distribution being a function of local flow depth; in reality, as the cross-sectional shape deforms, the cross-sectional mean velocity and the boundary shear stress associated with a given local flow depth would change. The assumption embodied herein is effectively that of a constant mean velocity (U) versus flow stage (h) relation at the cross section. Such an assumption varies from previous research on straight channel widening (Parker, 1978; Pizzuto, 1990; Kovacs and Parker, 1994), where linked hydrodynamic models were incorporated to allow the hydraulics to change as the channel shape changed. As in the case of the constant χ assumption, variation in the U versus h relationship associated with cross-section deformation cannot be made in a general way independent of the details of the hydrodynamics.

A final assumption pertains to time scales. The modeling proposed herein involves modeling the effects of a range of hydrographs over long time periods, during which time the U versus h relationship and χ remain constant. This yields lateral bank migration rates over a time scale that is longer than the time that the U versus h relationship and χ could be realistically expected to remain constant at a cross section. The assumption is that $\Delta\xi / \Delta t$ determined through this modeling effort scales down to smaller Δt intervals implemented in a hydrodynamic submodel such as RVR Meander-CONCEPTS.

8. Bank Erosion Submodel for Multiple-Hydrograph Time Scales

Because of the importance of history, a statistical approach must be combined with the physics-based modeling to yield the most probable value of $(\Delta\xi/\Delta t)_{\text{net}}$ associated with the flow duration curve. The current method involves several differences from the "model discharge" approach described in the previous section to best account for the importance of history on bank erosion: (a) $(\Delta\xi/\Delta t)_i$ will be determined for discretized ranges of hydrographs rather than discretized ranges of the flow duration curve; (b) the numerous possibilities of initial bank profile on which the hydrographs act will be evaluated. The details of the method are as follows:

1. Field Analysis
    a. Determine properties such as H_{bf}, H_{nc}, and H_{ar} describing the bank; determine D_{50} of bank material.
    b. Using Eq. (15), Determine the minimum flow stage h_{min} required to exceed τ^*_c at the toe of the bank for the maximum value of χ being evaluated, which corresponds to the location in a bend that experiences the maximum boundary shear stress; any flow rates yielding a stage lower than h_{min} are not relevant for the bank migration analysis.
2. Statistical Analysis of Flow Data
    a. Determine a representative Q versus h stage-discharge relationship in the project reach.
    b. Using stream gauge data with appropriate temporal resolution, assemble all the independent flood hydrographs generating h greater than h_{min} within the project reach. This yields N hydrographs each having a peak flow Q_{peak}.
    c. Discretize the range from $Q_{peak,min}$ to $Q_{peak,max}$ into an appropriate number of bins. The number of samples in each bin is referred to as n_i.
    d. Determine the total time t_i occupied by all the hydrographs in each bin.
    e. Generate a probability distribution where $p_{1,i} = n_i / N$. This is known as *Probability Distribution 1*. (This can also be generated by fitting an appropriate probability distribution function to the data.)
    f. Generate a probability distribution where $p_{2,i} = t_i / T_{record}$, where T_{record} is the total time of the entire gauge record. Note that $\sum p_{2,i}$ across all bins will not equal 1.0 in this case because much of the record was discarded due to $h < h_{min}$. This is known as *Probability Distribution 2*. (This can also be generated by fitting an appropriate probability distribution function to the data.)
    g. For each bin, generate a representative synthetic hydrograph. This process can be as statistically sophisticated as desired to match the shape of the natural hydrographs. Regardless of the complexity chosen for the synthetic

hydrograph, it needs to be scaled with respect to the work done by the flow. The instantaneous force on the bank is calculated by integration of the boundary shear stress over the bank; given the boundary shear distribution specified in this study, the force is proportional to 0.5(h - η_{base})^2. If the variable h_{loc} is defined as (h - η_{base}), then the synthetic hydrograph should yield an integration value $\int h_{loc}^2 dt$ that is representative of the hydrographs in the bin.

3. Numerical Simulations
    a. Set χ = 1 and determine $(\Delta\xi/\Delta t)_{\text{net}}$. The required steps to achieve that determination are outlined as follows.
        i. Generate a population of 'initial bank profiles'. This is done by performing bank erosion simulations of a large number of consecutive hydrographs, the sequence of which is selected randomly based on *Probability Distribution 1*. Output the bank profile after each hydrograph is completed.
        ii. Determine $(\Delta\xi/\Delta t)_i$ for the Bin 1 representative hydrograph. This is done by performing a simulation of the synthetic hydrograph on each of the 'initial bank profiles'. For each simulation, calculate ($\Delta\xi/\Delta t$) averaged over the hydrograph. Calculate the average ($\Delta\xi/\Delta t$) from all trials (each trial represents a different initial bank profile). Statistical analysis should be implemented to ensure that an appropriate number of initial bank profiles are run to converge on the proper value of $(\Delta\xi/\Delta t)_i$.
        iii. Repeat step (ii) to determine $(\Delta\xi/\Delta t)_i$ for all bins.
        iv. Find the $(\Delta\xi/\Delta t)_{\text{net}}$ associated with the current χ being evaluated. This is done by integrating $(\Delta\xi/\Delta t)_i$ with $p_{2,i}$ across all the bins.
        v. Find the "effective discharge" for this value of χ, which is the representative Q for the bin containing the maximum value of the product $p_{2,i}$ x $(\Delta\xi/\Delta t)_i$. Because this bin represents a full hydrograph of varying Q, the value should be chosen by determining the constant value h_{loc} such that h_{loc}^2 x T_{hyd} is equal to $\int h_{loc}^2 dt$ for the representative hydrograph in the bin. That characteristic value of h_{loc} can then be converted to Q using the stage-discharge relationship.
    b. Repeat step (a) for each χ to evaluate over the full range of χ.
4. Develop an equation for the bank erosion submodel.
    a. Plot $(\Delta\xi/\Delta t)_{\text{net}}$ versus χ. Fit a curve to this line.

b. Determine Q_{mod} using the effective discharge determined for each of the χ values in step 3(a)(v). If Q_{mod} varies for different χ evaluated, use the value associated with $\chi = 1$.

Example Case: Mackinaw River, Illinois

Step 1: Field investigations of the Mackinaw River yielded the following estimates for the modeling parameters: H_{bf} = 4.0 m; H_{nc} = 2.5 m; H_{ar} = 1.0 m; D_{50} = 15 mm. Estimates of longitudinal slope S_0 range from S_0 = 0.00070 (digitized from contours on 1:24000 USGS quadrangle) to S_0 = 0.00047 (from http://pubs.usgs.gov/wri/wri934076/stations/05568000.html). For the simulations herein, the larger S = 0.00070 is used. It is assumed that H_{ar} = 0 to provide a reference condition. It is estimated that ($h - \eta_{base}$) must be at least 1.3 m before motion can be initiated in non-cohesive material at the base of the bank with χ = 1. (For larger χ in the first bin thus chosen, the time-integrated net erosion distance is found to be negligible, so this is an appropriate minimum bin.) This corresponds to $Q \approx$ 42.5 m^3/s (1500 cfs) based on the stage-discharge relationship at USGS gage station 05568000, which is located approximately 15 km (river distance) upstream of the field site shown in Fig. 2.

Step 2: The Q versus h stage-discharge relationship is assumed to be identical at the field site as at the USGS gage station where the discharge data was obtained. The stage-discharge relationship could also readily be determined using a 1D step-backwater analysis if the gage station did not adequately represent the project reach.

Readily available gage station data at 15-minute intervals was available for the period between June 1988 and December 2012. The data indicate that the 1500 cfs threshold considered relevant in this example is exceeded approximately 15.2% of the time on the flow duration curve. Analysis of the data to develop a partial duration series of all independent 'events' having a peak discharge greater than 1500 cfs yielded a population of 179 events. The range of Q_{peak} values in this time period varied from 1500 cfs to 16,400 cfs. The population was separated into fifteen bins occupying 1000 cfs (e.g., 1500 to 2500 cfs; 2500 to 3500 cfs; etc.) *Probability Distribution 1* and *Probability Distribution 2* were developed as described, which are illustrated in the attached Figures 17 and 18.

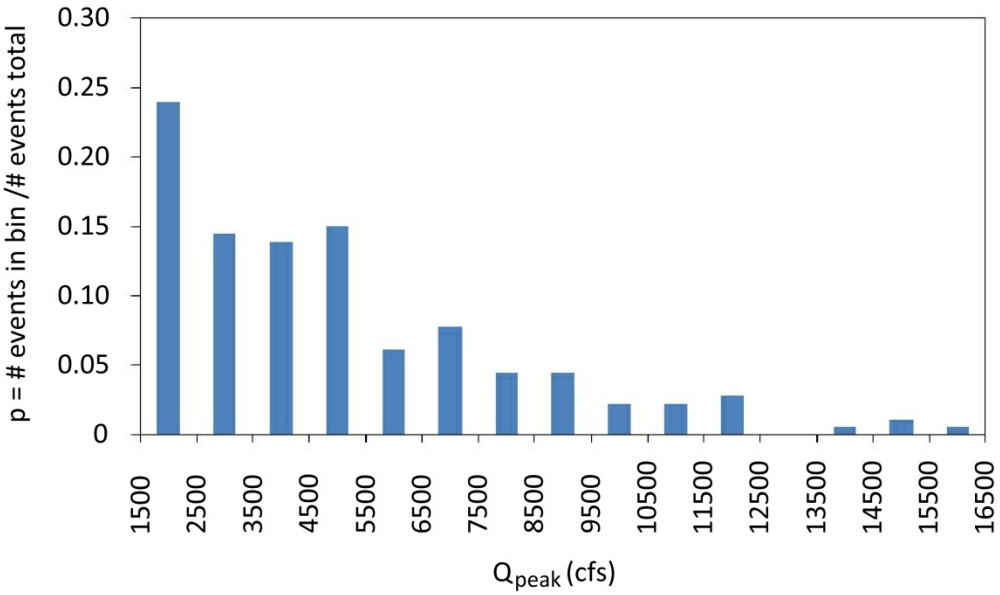

Figure 17: *Probability Distribution 1* for the 179 flow events on the Mackinaw River (USGS gage station 05568000) between June 1988 and December 2012.

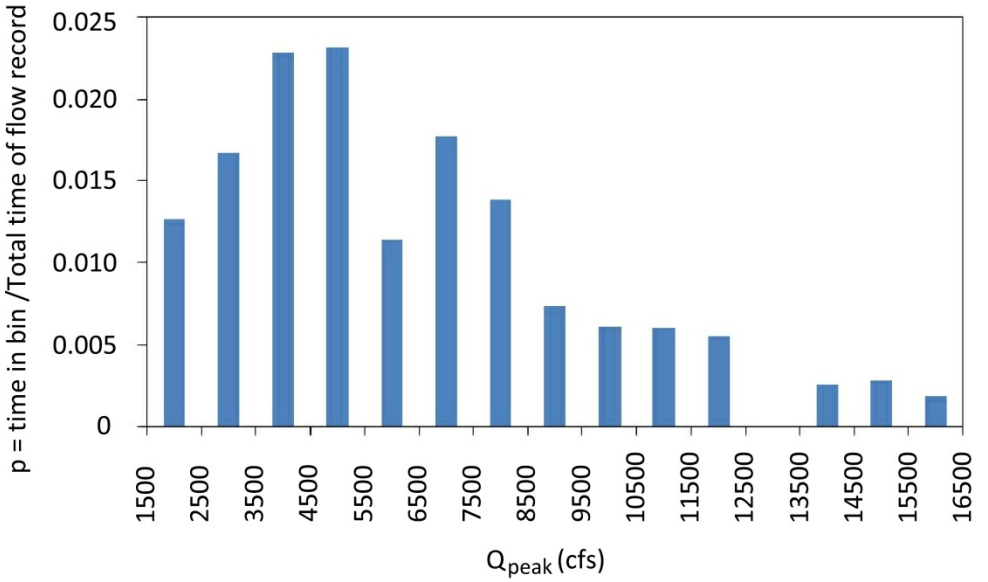

Figure 18: *Probability Distribution 2* determined for the same population of 179 events as shown above.

Although not specifically required in the methodology, the annual maxima series dating back to 1922 was analyzed. The annual maxima varied from 1830 cfs up to 51,000 cfs. Because the 24-year record of 15-minute resolution data did not contain the highest peaks on the annual series, this suggests that a probability distribution should probably be fit to the data to account for the full range of possible flood events. Functions were not fit to the data from Fig. 17 and 18, as this example is simply intended to illustrate the general

method. The median annual maximum (Q_{2yr}) was 8,120 cfs. This discharge corresponds closely to a discontinuity in the stage-discharge relationship at approximately 8,500 cfs; the bankfull discharge in the project reach is therefore likely in this range. The 24-year range of data includes 33 events exceeding the estimated bankfull discharge.

Synthetic hydrographs were represented for each bin, each scaled such that the value $\int h_{loc}^2 dt$ was representative of the actual discharge data from the gage station for the hydrographs in the bin. The method for creating the synthetic hydrographs is illustrated in Figure 19. The actual synthetic hydrographs used are shown in Figure 20.

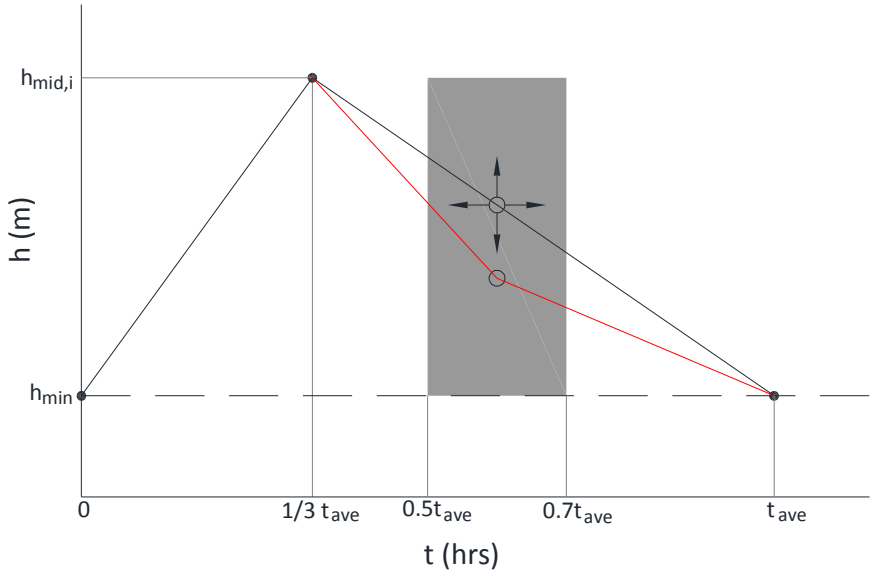

Figure 19: The method for creating the synthetic hydrographs. The synthetic hydrographs contain 4 points, 3 of which are fixed. The value t_{ave} is the average duration of the individual hydrographs in bin i; note that portions of the hydrograph where Q < 1500 cfs (associated with h_{min}) have been truncated. The first fixed hydrograph point is at t = 0 and h = h_{min}. The second fixed point is at t = 1/3t_{ave} and h = $h_{mid,i}$; the latter value is is associated with Q_{peak} equal to the midpoint of the bin; for example, in the bin containing hydrographs with Q_{peak} between 1500 and 2500 cfs, $h_{mid,i}$ is associated with Q = 2000 cfs). The third fixed point is at t = t_{ave} and h = h_{min}. The non-fixed point shown with the open circle is adjusted through an iterative procedure within the gray-shaded region such that the integration $\int h_{loc}^2 dt$ for the synthetic hydrograph equals the average value of $\sum h_{loc}^2 \Delta t$ calculated from the actual hydrographs in the bin.

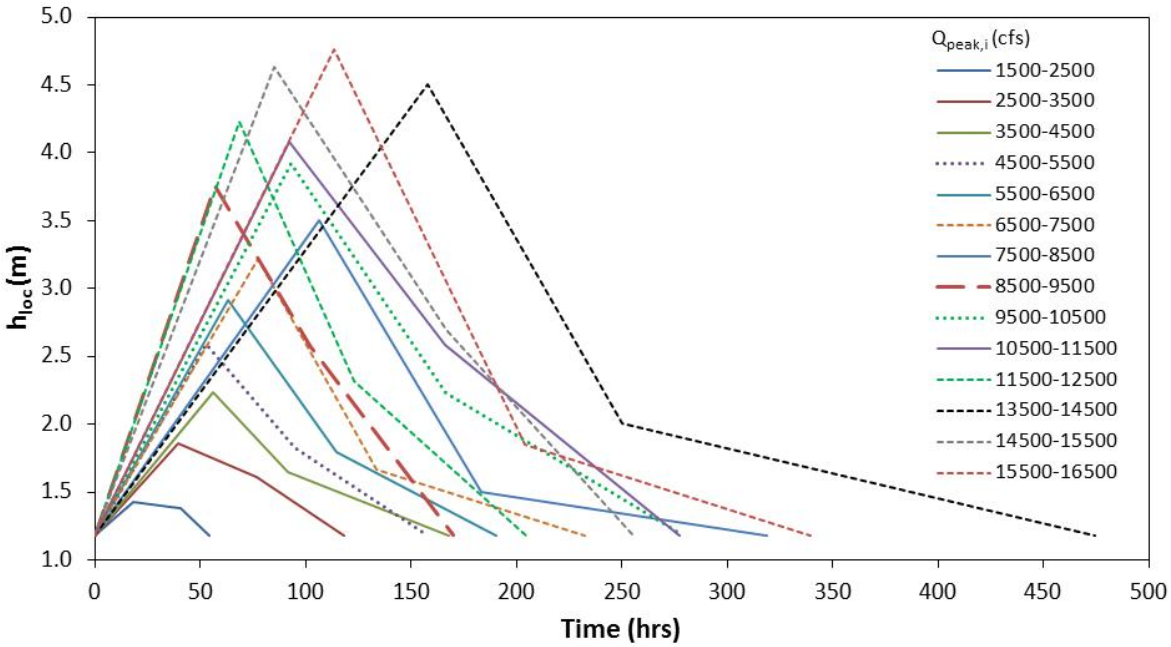

Figure 20: The synthetic hydrographs developed for the current analysis.

Step 3: For this analysis, four values of χ were evaluated: 0.5, 1.0, 1.5, and 2.0. A limited number of initial bank profiles were simulated, however they did cover the full range of expected initial bank profiles. An example of the calculation of $(\Delta\xi/\Delta t)_{net}$ associated with χ = 1 is illustrated in Figure 21.

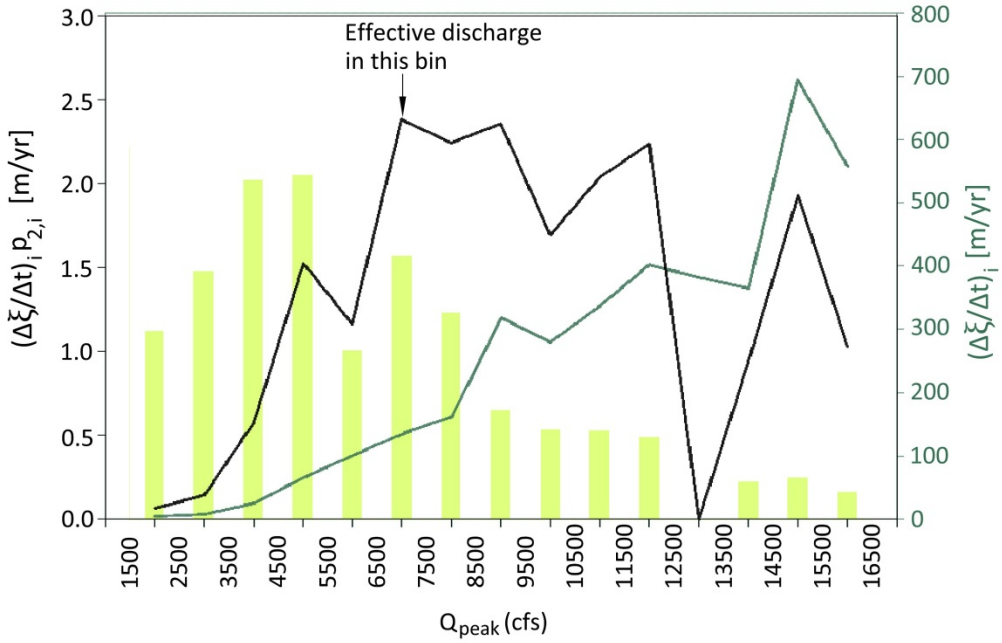

Figure 21: An example $(\Delta\xi/\Delta t)_{net}$ calculation for χ = 1. The green curve shows the simulation results of $(\Delta\xi/\Delta t)_i$ for each synthetic hydrograph (which is actually the average over the various initial bank profiles considered); the values of the green curve are measured on the secondary y-axis. The values of the yellow Probability Distribution 2 are not scaled on one of the y-axes, but the values can be found in Figure 18. The black curve is the product of $(\Delta\xi/\Delta t)_i$ for the bin and the associated probability per Probability Distribution 2; it is measured on the primary y-axis. The effective discharge is the peak of the black curve. Integration of the black curve over all the bins yields $(\Delta\xi/\Delta t)_{net}$. In this example, $(\Delta\xi/\Delta t)_{net}$ is equal to 20.3 meters/year.

Step 4: The same procedure shown in Figure 21 is performed for all the χ values in the analysis. The results are illustrated in Figure 22.

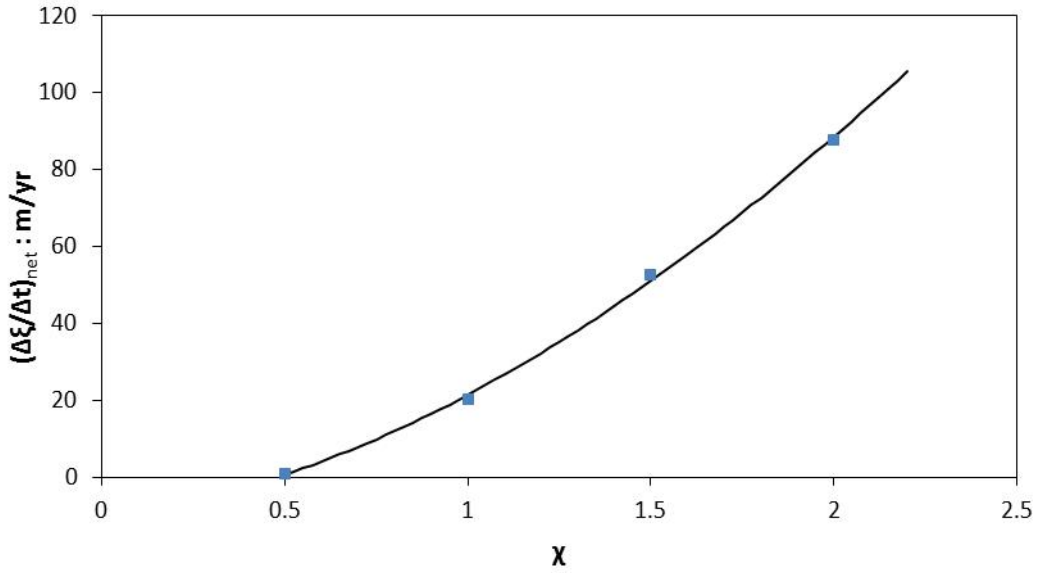

Figure 22: The final results of the bank erosion submodel for the Mackinaw River example case. The blue points are the numerical results; the black curve is a best-fit curve to the data points, described below.

As is evident from Fig. 22, the modeled predictions for the bank migration rate are approximately an order of magnitude too large, based on a brief analysis of aerial photographs in the project reach. The causes for the over-prediction are discussed in §9. Despite the over-prediction, a best-fit to the curve was found by assuming the following form for the equation:

$$\left(\frac{\Delta\xi}{\Delta t}\right)_{net} = m\chi^a + b \tag{22}$$

The parameters m, a, and b were found statistically by assuming a range of values for a, performing a linear regression to determine the values m and b for each a; and then selecting the value a that minimized the residual sum of squares between the modeled data points and the predicted value based on Eq. (20). The resulting equation is as follows:

$$\left(\frac{\Delta\xi}{\Delta t}\right)_{net} = \begin{cases} 0, & \text{for } \chi \leq 0.47 \\ 29.8\ \text{m/yr}(\chi)^{1.7} - 8.3\ \text{m/yr}, & \text{for } \chi > 0.47 \end{cases} \tag{23}$$

A formulation such as that of Eq. (23) can be readily incorporated as the bank erosion submodel in a numerical model of meandering river migration such as RVR Meander.

9. Discussion and Conclusions

The current study provides a methodology for developing a bank erosion submodel for composite river banks that can be linked to a hydrodynamic submodel, such as RVR Meander-CONCEPTS. The bank erosion submodel takes the form of a relation between $(\Delta\xi/\Delta t)_{\text{net}}$ versus χ, the latter of which is determined from the output of a hydrodynamic submodel. The relationship is developed by implementing numerical simulations that have a physical basis: coupled equations for 2D bedload transport on a steep side slope with the Exner equation of sediment mass continuity. A full range of hydrographs are simulated; and the submodel can be readily modified to account for a modified flow regime by modifying the characteristics of the hydrographs or their probability distribution. To the best of the authors' knowledge, such a capability to account for modified hydrologic regime is unique with respect to available bank erosion models.

The over-prediction of the bank migration rate $(\Delta\xi/\Delta t)_{\text{net}}$ in the Mackinaw River example case is primarily based on two factors: (a) not accounting for the armoring associated with failed cohesive material derived from the upper bank layer; (b) not accounting for modifications to τ_{bank} associated with bank roughness form drag and large woody debris; (c) not accounting for increased bank resistance to fluid shear stress due to live vegetation; (d) not accounting for the influence of structured deposits forming the banks. The first issue can be resolved in part by utilizing the modeling techniques illustrated in this study, whereby a portion of the base is rendered immobile. This has been shown to influence the migration rate at the top of the non-cohesive layer. The technique used in this study specifies H_{ar} as a parameter; a more sophisticated approach could be implemented to dynamically introduce armoring as the upper cohesive layer was undercut. Early forms of such an approach are described by Parker et al (2011). In the Mackinaw River example, the simulations for χ = 1 (the reach-average value) with a hydrograph having an average recurrence interval of approximately 4 years on the annual series (Q_{peak} = 14,500) yielded bank migration of over 20 meters during a single event; when χ was increased to 1.5, bank migration increased to approximately 40 meters during a single event. Such migration would deliver enormous amounts of upper bank material into the river, a portion of which would likely be retained near the bank toe. Furthermore, the large load of non-cohesive bank sediment would likely aggrade the river bed; and the widening of the cross-section by approximately 50% of the bank-full width would affect the hydraulics and boundary shear stress. It appears that without considering the basal armoring, a physically-based model of non-cohesive bank erosion will over-predict migration rates in composite-bank rivers. The second and third factors associated with bank roughness and vegetation will be difficult to resolve in a mechanistic approach. The final factor resulting in over-prediction pertains to the influence of structured deposits to mitigate migration rates; this issue is also not so readily resolved. Research does not exist regarding the entrainment of structured deposits and

equilibrium bedload transport rates on very steep side slopes which have been observed in banks of structured non-cohesive soil. One potential approach would be simply to assume an increased $\tau^*_{c,0}$ and that standard bedload formulations are otherwise relevant; then the approach for bedload transport on steep side slopes implemented in this study could be used. However, such an approach cannot currently be substantiated with field or laboratory data.

Although the bank migration rate in the Mackinaw River case is over-predicted by approximately an order of magnitude, the finding that the migration rate is non-linear with respect to the boundary shear stress, represented through the parameter χ, is important. The non-linear relationship likely leads to meander development that could not be captured in physically-based modeling of fluvial erosion of non-cohesive material using a linear formulation similar to Eq. (1).

In addition to the practical benefit of the findings for meandering river migration models, some fundamental insights regarding deformation of non-cohesive banks are provided. Bank material mobilized as bedload according to the given boundary shear stress distribution will generally tend toward a concave bank profile with a low transverse slope at the base. The simulations reveal that the magnitude of the bank retreat is highly sensitive to the initial concavity of the bank profile. When a bank is initially steep down to the base, the upper bank deformation is accelerated during the initial development of concavity. As such, the presence of basal material situated at a low angle at the toe of the bank is very important in mitigating bank retreat even if that material is mobile during a flow event. In this circumstance, strong differentials in $q_{s,y}$ do not initially exist across the bank profile, which explains the reduced rate of deformation. In the case where the thalweg of a river is migrating into the eroding bank, and the low-angle basal material is removed through development of strong $q_{s,x}$ gradients in the bed region, this clearly accelerates bank erosion through the process described above, even if the thalweg is not becoming deeper. This scenario is not accounted for in the current numerical model. The influence of basal armoring is most pronounced in Type 2 and Type 3 deformation under an initially steep slope; much like the case of the low angle basal material, the basal armoring influence is also due to preventing the strong concavity from developing at the base that feeds back to influence deformation higher up the bank.

After development of the concave bank profile, bank deformation persists because an equilibrium profile cannot develop when $q_{s,y} = 0$ at the interface where $(\tau^*/\tau^*_c) = 1$ and $q_{s,y} > 0$ lower on the bank. In a straight channel, the hydrodynamics adjust as the bank widens, and eventually a static equilibrium prevails where $q_{s,y} = 0$ across the entire bank profile. In the case of a migrating bank at a meander bend, where a high velocity core may maintain close proximity to the outer bank during bank deformation, such a static equilibrium does not develop. The current numerical model does not account for modification of the cross-sectional

hydraulics (the U versus h relationship) during bank deformation. Modification of hydraulics is incorporated through linkage to a hydrodynamic submodel such as RVR Meander-CONCEPTS.

The numerous simulations of the Mackinaw River reveal a dominant general pattern of bank erosion: large events have a strong tendency to cause reduction in bank slope and bank migration through Type 2 or Type 3 deformation; small events generally cause minimal bank migration, and primarily serve to steepen portions of the lower bank; this may be considered a rejuvenation of the steepness of portions of the lower slope. It is expected that in most composite-banked rivers in which the ratio of H_{nc} to H_{bf} is large (greater than about 0.5) that this general pattern will prevail. In cases where the ratio of H_{nc} to H_{bf} is small, then Type 1 deformation will become more important. The general dominant pattern of bank erosion described above support the findings of Pizzuto (1994) where bank migration and channel widening followed a large flood event, and during intermediate higher frequency flood events, bank migration was minimal and deposition within the channel, in particular on the point bar, became more prevalent than bank erosion. Such a sequence may be very important for maintaining the single-thread channel form in rivers having banks comprised of non-cohesive sediment, as suggested by Parker et al (2011). That study included a discussion of the difficulty in achieving a single-thread meandering channel form in a laboratory setting where the channel is allowed to evolve in a floodplain of non-cohesive sediments. Although previous research has suggested that some form of cohesion is required to achieve the single-thread meandering plan-form, the current study suggests that careful regulation of the experimental flow regime should be investigated as a potential means of allowing the single-thread form to exist in the laboratory. For example, a single flow that is maintained indefinitely at or near the effective discharge will certainly continually decrease the slope of the eroding bank, causing the channel to widen and shallow. Time scales relevant to bank migration should also be carefully considered; scaling the appropriate time from field prototype scale to the model scale is readily accomplished with the non-dimensional form of the Exner equation used.

Notation

The following symbols are used in this report:

a : arbitrary exponent used in evaluation of power laws

b: arbitrary y-intercept used in evaluation of linear formulations

C_1 : dimensionless parameter used in the non-dimensional Exner equation

C_2 : dimensionless parameter used in the non-dimensional Exner equation

D_{50} : median sediment diameter in the grain-size distribution [L]

E : dimensionless bank migration coefficient

g : gravitational acceleration constant [L/T^2]

h : instantaneous flow stage, or water surface elevation [L]

h^* : dimensionless form of h

h_{loc} : local flow depth; equal to h - η_{base} [L]

h_{min} : minimum flow stage required to initiate sediment motion at the base of the bank [L]

H_{ar}: local depth of basal armoring, or vertical distance from toe of bank to top of armor [L]

H_{bf} : local bank-full depth, or vertical distance from toe of bank to top of bank [L]

H_{nc}: local depth of non-cohesive sediment layer, or vertical distance from toe of bank to top of non-cohesive layer [L]

i : numerical node with respect to the numerical model; a specific bin of a discretized flow duration curve with respect to determination of model discharge

I_{mod} : intermittency of Q_{mod} used in the hydrodynamic submodel

K : slope factor; equivalent to τ^*_c / τ^*_{c0}

k_d : erodibility coefficient [L^2T/M]

m : slope of fitted linear formulation

M : erosion-rate coefficient [L/T]

n : distance along the transverse coordinate (normal to streamwise coordinate) in a curvilinear coordinate system [L]

N : number of bins used in the evaluation of probability distribution of historic discharge

Δp_i : the probability of occurrence of a specific bin i determined from the flow duration curve

q_s : volumetric sediment transport rate per unit width along the resultant direction of transport on the inclined plane of the bank [L^2/T]

$q_{s,n}$: volumetric sediment transport rate per unit width along the transverse coordinate (normal to the streamwise coordinate) [L^2/T]

$q_{s,s}$: volumetric sediment transport rate per unit width along the streamwise coordinate [L^2/T]

$q_{s,x}$: volumetric sediment transport rate per unit width along the streamwise Cartesian coordinate [L^2/T]

$q_{s,y}$: volumetric sediment transport rate per unit width along the transverse Cartesian coordinate [L^2/T]

$q_{s,y'}$: volumetric sediment transport rate per unit width in the transverse direction on the inclined plane of the bank [L^2/T]

$q^*_{s,x}$: volumetric sediment transport rate per unit width along the streamwise Cartesian coordinate [L^2/T]

Q : volumetric flow rate [L^3/T]

Q_{mod} : volumetric flow rate modeled in the hydrodynamic submodel that best represents long time scales [L^3/T]

Q_{peak} : the peak Q of an individual hydrograph [L^3/T]

R : submerged specific gravity of sediment

s : distance along the streamwise coordinate in a curvilinear coordinate system [L]

S_0 : reach-averaged longitudinal bed slope [L/L]

t : time [T]

t^* : dimensionless time

T_{hyd} : duration of modeled hydrograph, used in non-dimensionalization of time [T]

T_{record} : time incorporated in the entire flow record used in the statistical analysis [T]

U : cross-sectional mean flow velocity [L/T]

u' : near-bank excess velocity [L/T]

x : distance along the streamwise direction in the Cartesian coordinate system [L]

y : distance along the transverse direction in the Cartesian coordinate system [L]

y^* : dimensionless form of y

y' : distance in the transverse direction on the inclined plane of the bank [L]

z : distance along the vertical direction in the Cartesian coordinate system [L]

β : deviation angle on the inclined plane of the sediment transport direction relative to the flow direction

γ : intermediate variable that expresses a term in the dimensionless Exner equation

ε : fluvial erosion rate [L/T]

η : bed/bank elevation above an arbitrary datum [L]

η^* : dimensionless form of η

η_{base} : the value of η at the base of the bank [L]

θ_{rm} : mass angle of repose

θ_{rp} : particle angle of repose

λ : soil porosity, or volume pore space divided by total soil volume

μ : dynamic friction coefficient

μ_s : static friction coefficient

$\Delta\xi$: lateral bank migration distance measured at the top of bank [L]

ρ : density of water [M/L^3]

ρ_s : density of sediment [M/L^3]

τ_b : boundary shear stress [M/L/T^2]

τ_c : critical boundary shear stress required to initiate sediment motion [M/L/T^2]

τ^* : dimensionless boundary shear stress, or Shields' parameter

τ^* : dimensionless boundary shear stress

τ^*_{base} : dimensionless boundary shear stress at the base of the bank

τ^*_c : dimensionless critical boundary shear stress on an arbitrary slope

τ^*_{c0} : dimensionless critical boundary shear stress for a flat bed

τ^*_{ref} : reference value of τ^*_{base} determined from reach-averaged channel properties

Φ : friction angle, or angle of internal friction

Φ_i : angle of initial yield

χ : constant that parameterizes local deviation of boundary shear stress relative to the reach-averaged value; equal to $\tau^*_{base} / \tau^*_{ref}$

ω : local transverse slope angle

Acknowledgments

This research was funded through a grant from the Illinois Water Resource Center. Davide Motta of the Ven Te Chow Hydrosystems Laboratory at the University of Illinois in Urbana-Champaign is also gratefully acknowledged for many helpful discussions and suggestions.

References

Abad, J.D., M.H. Garcia, 2006, RVR Meander: A toolbox for re-meandering of channelized streams. *Computers & Geosciences*, 32(1), 92-101.

Allen, J.R.L., 1970, The avalanching of granular solids on dune and similar slopes, *The Journal of Geology*, 326-351.

Arulanandan, K., E. Gillogley, R. Tully, 1980, Development of a quantitative method to predict critical shear stress and rate of erosion of natural undisturbed cohesive soils, *Rep. GL-80-5*, U.S. Army Corps of Eng., Waterways Exp. Station, Vicksburg, Miss.

Carrigy, M.A., 2006, Experiments on the angles of repose of granular materials, *Sedimentology*, 14(3-4), 147-158.

Constantine, C.R., T. Dunne, G.J. Hanson, 2009, Examining the physical meaning of the bank erosion coefficient used in meander migration modeling, *Geomorphology*, 106(3), 242-252.

Daerr, A., S. Douady, 1999, Two types of avalanche behaviour in granular media, *Nature*, 399(6733), 241-242.

Darby, S.E., A.M. Alabyan, M.J. Van de Wiel, 2002, Numerical simulation of bank erosion and channel migration in meandering rivers, *Water Resources Research*, 38(9), 1163.

Darby, S.E., M. Rinaldi, S. Dapporto, 2007, Coupled simulations of fluvial erosion and mass wasting for cohesive river banks, *Journal of Geophysical Research*, 112(F3), F03022.

Eagleson, P.S., R.G. Dean, 1959, Wave-induced motion of bottom sediment particles, *Journal of the Hydraulics Division*, 85(10), 53-79.

Engelund, F., 1974, Flow and bed topography in channel bends, *Journal of Hydraulic Research*, 100(11), 1631–1648.

Engelund, F., J. Fredsoe, 1976, A sediment transport model for straight alluvial channels, *Nordic Hydrology*, 7, 293–306.

Fernandez-Luque, R., R. Van Beek, 1976, Erosion and transport of bed-load sediment, *Journal of Hydraulic Research*, 14(2), 127-144.

García, M.H., 2008, Sediment transport and morphodynamics, in M.H. García, ed., *ASCE manual of practice 110—Sedimentation engineering: Processes, measurements, modeling, and practice*, ASCE, Reston,VA, 21–163.

Glover, R.E., Q.L. Florey, 1951, *Stable Channel Profiles*, U.S. Bureau of Reclamation, Hydraulics, 325.

Hanson, G.J., 1990, Surface erodibility of earthen channels at high stresses. Part II: developing an in situ testing device, *Transactions of the ASAE*, 33(1), 132-137.

Hanson, G.J., K.R. Cook, 2004, Apparatus, test procedures, and analytical methods to measure soil erodibility in situ, *Appl. Eng. Agric.*, 20, 455–462.

Hasegawa, K., 1977, Computer simulation of the gradual migration of meandering channels, *Proceedings of the Hokkaido Branch, Japan Society of Civil Engineering*, 197–202 (in Japanese).

Hasegawa, K., 1981, Bank-erosion discharge based on a non-equilibrium theory, *Proc. JSCE, Tokyo*, 316, 37–50 (in Japanese).

Hasegawa, K., 1989, Universal bank erosion coefficient for meandering rivers, *Journal of Hydraulic Engineering*, 115(6), 744-765.

Ikeda, S., 1982, Incipient motion of sand particles on side slopes, *Journal of the Hydraulics Division*, 108(1), 95-114.

Ikeda, S., G. Parker, K. Sawai, 1981, Bend theory of river meanders. Part 1. Linear development, *Journal of Fluid Mechanics*, 112(11), 363-377.

Jang, C.L., Y. Shimizu, 2005, Numerical simulation of relatively wide, shallow channels with erodible banks, *Journal of Hydraulic Engineering*, 131(7), 565-575.

Johannesson H., G. Parker, 1985, Computer simulated migration of meandering rivers in Minnesota, *Project Report No. 242*, University of Minnesota, St. Anthony Falls Hydraulic Laboratory, Minneapolis, Minnesota.

Kirchner, J.W., W.E. Dietrich, F. Iseya, H. Ikeda, 2006, The variability of critical shear stress, friction angle, and grain protrusion in water-worked sediments, *Sedimentology*, 37(4), 647-672.

Kothyari, U.C., R.K. Jain, 2008, Influence of cohesion on the incipient motion condition of sediment mixtures, *Water Resources Research*, 44(4), W04410.

Kovacs, A., G. Parker, 1994, A new vectorial bedload formulation and its application to the time evolution of straight river channels, *Journal of Fluid Mechanics*, 267, 153-183.

Langendoen, E.J., A. Simon, 2008, Modeling the evolution of incised streams. II: Streambank erosion, *Journal of Hydraulic Engineering*, 134(7), 905-915.

Langendoen, E.J., R.R. Wells, R.E. Thomas, A. Simon, R.L. Bingner, 2009, Modeling the evolution of incised streams. iii: Model application, *Journal of Hydraulic Engineering*, 135(6), 476-486.

Leroueil, S., P.R. Vaughan, 1990, General and congruent effects of structure in natural soils and weak rocks, *Geotechnique*, 40(3), 467-488.

Li, Z., P.D. Komar, 1986, Laboratory measurements of pivoting angles for applications to selective entrainment of gravel in a current, *Sedimentology*, 33(3), 413-423.

Lundgren, H., I.G. Jonsson, 1964, Shear and velocity distribution in shallow channels, *J. Hydraul. Div., Am. Soc. Civ. Eng*, 90(1), 1-21.

Millar, R.G., 2000, Influence of bank vegetation on alluvial channel patterns, *Water Resources Research*, 36(4), 1109-1118.

Millar, R.G., M.C. Quick, 1993, Effect of bank stability on geometry of gravel rivers, *Journal of Hydraulic Engineering*, 119(12), 1343-1363.

Miller, R.L., R.J. Byrne, 2006, The angle of repose for a single grain on a fixed rough bed, *Sedimentology*, 6(4), 303-314.

Mitchener, H., H. Torfs, 1996, Erosion of mud/sand mixtures, *Coastal Engineering*, 29(1), 1-25.

Motta, D., J.D. Abad, E.J. Langendoen, M.H. Garcia, 2012a, A simplified 2D model for meander migration with physically-based bank evolution, *Geomorphology*, 163, 10-25.

Motta, D., J.D. Abad, E.J. Langendoen, M.H. Garcia, 2012b, The effects of floodplain soil heterogeneity on meander planform shape, *Water Resources Research*, 48(9), W09518.

Nagata, N., T. Hosoda, Y. Muramoto, 2000, Numerical analysis of river channel processes with bank erosion, *Journal of Hydraulic Engineering*, 126(4), 243-252.

Nasermoaddeli, M.H., E. Pasche, 2010, Modelling of undercutting and failure of non-cohesive riverbanks, in Dittrich, A., K. Koll, J. Aberle, P. Gaisenhainer eds., *River Flow 2010: proceedings of the International Conference on Fluvial Hydraulics*, BAW 2010, Braunschweig, Germany, 1323-1330.

Panagiotopoulos, I., G. Voulgaris, M.B. Collins, 1997, The influence of clay on the threshold of movement of fine sandy beds, *Coastal Engineering*, 32(1), 19-43.

Parker, G., 1978, Self-formed straight rivers with equilibrium banks and mobile bed, Part 2, The gravel river, *J. Fluid Mech*, 89(1), 127-146.

Parker, G., Y. Shimizu, G.V. Wilkerson, E.C. Eke, J.D. Abad, J.W. Lauer, C. Paola, W.E. Dietrich, V.R. Voller, (2011). A new framework for modeling the migration of meandering rivers. *Earth Surface Processes and Landforms*, 36(1), 70-86.

Partheniades, E., 1965, Erosion and deposition of cohesive soils, *Journal of the Hydraulics Division, ASCE*, 91(1), 105-139.

Pizzuto, J.E., 1990, Numerical simulation of gravel river widening, *Water Resources Research*, WRERAQ, 26(9), 1971-1980.

Pizzuto, J.E., 1994, Channel adjustments to changing discharges, Powder River, Montana, *Geological Society of America Bulletin*, 106(11), 1494-1501.

Powell, D.M., P.J. Ashworth, 1995, Spatial pattern of flow competence and bed load transport in a divided gravel bed river, *Water Resources Research*, 31(3), 741-752.

Rüther, N., N.R.B. Olsen, 2007, Modelling free-forming meander evolution in a laboratory channel using three-dimensional computational fluid dynamics, *Geomorphology*, *89*(3), 308-319.

Schaffernak, F., (1916), Die theorie des geschiebebetriebes und ihre Anwendung, *Zeitschrift des Oesterreichischen Ingenieur und Architeken-Vereines*, Vienna, Austria, 1916.

Terzaghi, K., R.B. Peck, G. Mesri, 1996, *Soil mechanics in engineering practice*, Wiley-Interscience, New York.

Thorne, C.R., 1982, Processes and mechanisms of river bank erosion, in R.D. Hey, J.C. Bathurst, C.R. Thorne eds, *Gravel-bed Rivers*, Wiley, Chichester, 227–271.

Thorne, C.R., N.K. Tovey, 1981, Stability of composite river banks, *Earth Surface Processes and Landforms*, 6(5), 469-484.

Van Burkalow, A., 1945, Angle of repose and angle of sliding friction: an experimental study, *Geological Society of America Bulletin*, 56(6), 669-707.

Wallick, J.R., S.T. Lancaster, J.P. Bolte, 2006, Determination of bank erodibility for natural and anthropogenic bank materials using a model of lateral migration and observed erosion along the Willamette River, Oregon, USA, *River Research and Applications*, 22(6), 631-649.

Wiberg, P.L., J.D. Smith, 1987, Calculations of the critical shear stress for motion of uniform and heterogeneous sediments, *Water Resources Research*, 23(8), 1471-1480.

Wolman, M.G., J.P. Miller, 1960, Magnitude and frequency of forces in geomorphic processes, *The Journal of Geology*, 54-74.

Wood, A.L., A. Simon, P.W. Downs, C.R. Thorne, 2001, Bank-toe processes in incised channels: the role of apparent cohesion in the entrainment of failed bank materials. *Hydrological Processes*, 15(1), 39-61.

Appendix A

Derivation of the parameter β used for transverse bedload component

Note: Derivation from Marcelo H. Garcia, originally prepared in 1990; amended by Davide Motta in 2011; amended by David Waterman in 2013.

1 Definitions

General vectors and coordinates

$\vec{i}, \vec{j}, \vec{k}$ = streamwise tangential, transverse tangential, upward normal unit vectors

s = streamwise tangential coordinate (in $\vec{i}$ direction)

n = transverse tangential coordinate (in $\vec{j}$ direction)

ϖ = side angle (the streamwise slope is assumed small)

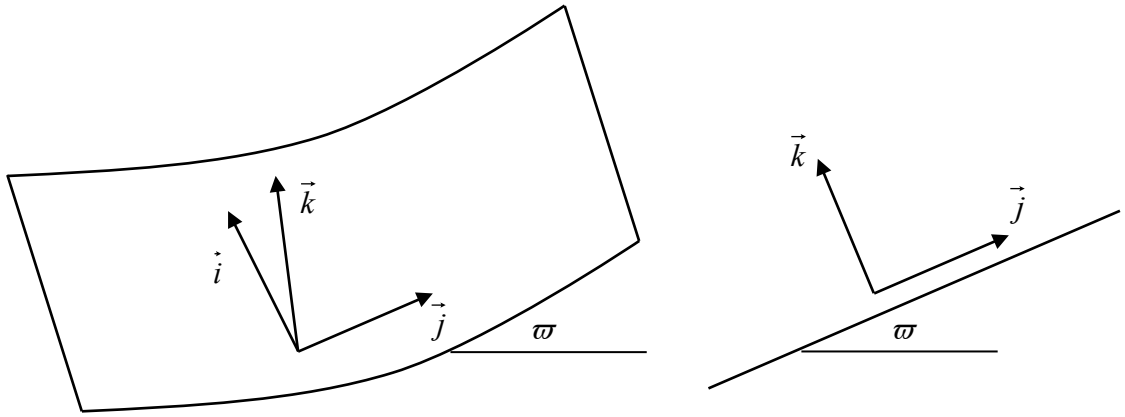

3D view ***Side view***

Gravitational vector

$$\vec{g} = -g\left(\cos\omega\vec{k} + \sin\omega\vec{j}\right) \tag{A1}$$

Bedload and bed particle velocity vectors

Bedload vector

$$\vec{q} = q_s\vec{i} + q_n\vec{j} \tag{A2a}$$

Bed particle velocity vector

$$\overrightarrow{v_p} = v_{ps}\vec{i} + v_{pn}\vec{j} \tag{A2b}$$

We can write

$$\beta = \tan^{-1}\left(\frac{q_n}{q_s}\right) = \tan^{-1}\left(\frac{v_{pn}}{v_{ps}}\right) \tag{A2c}$$

and

$$\overrightarrow{v_p} = v_{ps}\left(\vec{i} + \tan\beta\vec{j}\right) \tag{A2d}$$

Vectors of bed shear stress and near-bed velocity

Bed shear stress

$$\vec{\tau} = \tau_s\vec{i} + \tau_n\vec{j} \tag{A3a}$$

Near-bed velocity

$$\overrightarrow{u_b} = u_{bs}\vec{i} + u_{bn}\vec{j} \tag{A3b}$$

We can write

$$\delta = \tan^{-1}\left(\frac{\tau_n}{\tau_s}\right) = \tan^{-1}\left(\frac{u_{bn}}{u_{bs}}\right) \tag{A3c}$$

From logarithmic law, there exists a value a such that

$$a\left|\vec{\tau}\right| = \rho\left|\overrightarrow{u_b}\right|^2 \tag{A3d}$$

From (3c) and (3d), it is found that

$$a\tau_s = \rho u_{bs}\left(u_{bs}^2 + u_{bn}^2\right)^{1/2} = \rho u_{bs}^2\left(1 + \tan^2\delta\right)^{1/2} \tag{A3e}$$

Vector of particle weight

$$\overrightarrow{W} = -W\left(\cos\varpi\vec{k} + \sin\varpi\vec{j}\right) \tag{A4a}$$

where

$$W = \frac{4}{3}\pi\left(\frac{D}{2}\right)^3\rho Rg \tag{A4b}$$

where

$$R = \frac{\rho_s}{\rho} - 1 \tag{A4c}$$

and D is the grain diameter.

Vectorial drag force on moving grain (averaged over saltations)

$$\overrightarrow{F_D} = F_{Ds}\vec{i} + F_{Dn}\vec{j} = \frac{1}{2}\rho c_D \pi\left(\frac{D}{2}\right)^2 \left(\overrightarrow{u_b} - \overrightarrow{v_p}\right)\left|\overrightarrow{u_b} - \overrightarrow{v_p}\right| \tag{A5a}$$

and

$$\delta^* = \tan^{-1}\left(\frac{F_{Dn}}{F_{Ds}}\right) = \tan^{-1}\left(\frac{u_{bn} - v_{pn}}{u_{bs} - v_{ps}}\right) \tag{A5b}$$

Dynamic Coulomb resistive force on grain

$$\overrightarrow{F_R} = -\mu W \cos\varpi\left(\cos\beta\vec{i} + \sin\beta\vec{j}\right) \tag{A6}$$

---

2 Notes

We ignore lift. The original Parker and Andrews (1985) relation reduces to

$$\tan\beta = \tan\delta - \frac{1}{\mu}\left(\frac{\tau^*_{co}}{\tau^*}\right)^{1/2}\tan\varpi \tag{A7a}$$

where

$$\tau^* = \frac{\tau_s}{\rho RgD} \tag{A7b}$$

and τ^*_{co} is he critical value of τ^* for ω = 0. The relation (A7a) is good only for ω << 1. The goal here is to generalize it to the case $\omega \le \omega_R$ where ω_R denotes the angle of repose.

---

3 Force balance on a moving grain

The force balance on a moving grain is written as

$$\overrightarrow{F_D} - W\vec{j}\sin\omega + \overrightarrow{F_R} = 0 \tag{A8a}$$

In the streamwise direction ($\vec{i}$)

$$\frac{1}{2}\rho c_D \pi \left(\frac{D}{2}\right)^2 \left(u_{bs} - v_{ps}\right)\left|\overrightarrow{u_b} - \overrightarrow{v_p}\right| = \frac{4}{3}\rho R g \pi \left(\frac{D}{2}\right)^3 \mu \cos\omega\cos\beta \tag{A8b}$$

where the LHS is F_{Ds}.

In the transverse direction ($\vec{j}$)

$$\frac{1}{2}\rho c_D \pi \left(\frac{D}{2}\right)^2 \left(u_{bn} - v_{pn}\right)\left|\overrightarrow{u_b} - \overrightarrow{v_p}\right| - \frac{4}{3}\rho R g \pi \left(\frac{D}{2}\right)^3 \sin\omega = \frac{4}{3}\rho R g \pi \left(\frac{D}{2}\right)^3 \mu \cos\omega\sin\beta \tag{A8c}$$

where the first term in the LHS is F_{Dn}.

A useful identity is

$$\frac{u_{bn} - v_{pn}}{u_{bs} - v_{ps}} = \frac{u_{bs}\tan\delta - v_{ps}\tan\beta}{u_{bs} - v_{ps}} \tag{A9}$$

---

4 Application to critical conditions on a side slope

At critical conditions

$$\mu = \mu_s \tag{A10}$$

where μ_s denotes the static value of μ, and

$$\overrightarrow{v_p} = 0 \tag{A11}$$

It follows, from (3c) and (5b), that

$$\delta^* = \delta \tag{A12}$$

Furthermore, we define τ_c such that

$$\tau_c = \left|\vec{\tau}\right|_{critical} = \sqrt{\tau_s^2 + \tau_n^2}\Big|_{critical} \tag{A13}$$

Taking the absolute value of (A8a), we have

$$\left(F_{Ds}\right)^2 + \left(F_{Dn} - W\sin\varpi\right)^2 = \left(\mu_s W\cos\varpi\right)^2 \tag{A14}$$

With (A4b), (A5a), (A11), and (A12), the above relation becomes

$$\left[u_{bs}\left|\vec{u_b}\right|\right]^2 + \left[u_{bs}\left|\vec{u_b}\right| - \frac{4}{3c_D}RgD\sin\omega\right]^2 = \left[\mu_s\frac{4}{3c_D}RgD\cos\omega\right]^2 \tag{A15}$$

Note further, from (A3d) and (A13), that

$$a\frac{\tau_c}{\rho}\left(\cos\delta,\sin\delta\right) = \left(u_{bs}\left|\vec{u_b}\right|, u_{bn}\left|\vec{u_b}\right|\right) \tag{A16}$$

Reducing (A15) with (A16)

$$\left[\tau_c^*\cos\delta\right]^2 + \left[\tau_c^*\sin\delta - \frac{4}{3c_D a}\sin\omega\right]^2 = \left[\mu_s\frac{4}{3c_D a}\cos\omega\right]^2 \quad where \quad \tau_c^* = \frac{\tau_c}{\rho RgD} = \frac{\left|\vec{\tau}\right|_{critical}}{\rho RgD} \tag{A17}$$

Now let τ_{co}^* denote the value of τ_c^* for $\omega = 0$. It is seen from (A17) that

$$\tau_{co}^* = \frac{4\mu_s}{3c_D a} \tag{A18}$$

Rewriting (A17)

$$\left[\frac{\tau_c^*}{\tau_{co}^*}\cos\delta\right]^2 + \left[\frac{\tau_c^*}{\tau_{co}^*}\sin\delta - \frac{1}{\mu_s}\sin\omega\right]^2 = \left[\cos\omega\right]^2 \tag{A19}$$

This is a straightforward generalization of the formula for $\delta = 0$.

Note in the above relation that $\tau_c^*/\tau_{co}^* \to 0$ as $\tan\omega \to \mu_s$, i.e., $\omega \to \omega_R$ where

$$\omega_R = \tan^{-1}\mu_s \tag{A20}$$

---

5 Application to moving particle on a side slope

(A8b) and (A8c) reduce to

$$\left(u_{bs}-v_{ps}\right)\left|\overrightarrow{u_b}-\overrightarrow{v_p}\right|=\frac{4}{3c_D}RgD\mu\cos\omega\cos\beta \tag{A21}$$

$$\left(u_{bn}-v_{pn}\right)\left|\overrightarrow{u_b}-\overrightarrow{v_p}\right|=\frac{4}{3c_D}RgD\sin\omega+\frac{4}{3c_D}RgD\mu\cos\omega\sin\beta \tag{A22}$$

Dividing (A22) by (A21) and using (A5b)

$$\tan\delta^*=\tan\beta+\frac{1}{\mu}\frac{\tan\omega}{\cos\beta} \tag{A23}$$

Now (A5a) and (A5b) yield

$$\left|\overrightarrow{u_b}-\overrightarrow{v_p}\right|=\left[\left(u_{bs}-v_{ps}\right)^2+\left(u_{bn}-v_{pn}\right)^2\right]^{1/2}=\left[1+\tan^2\delta^*\right]^{1/2}\left(u_{bs}-v_{ps}\right) \tag{A24}$$

(A21) thus becomes

$$\left(u_{bs}-v_{ps}\right)^2=\frac{4\mu}{3c_D}\frac{RgD}{\left[1+\tan^2\delta^*\right]^{1/2}}\cos\omega\cos\beta \tag{A25a}$$

or, reducing with (A18)

$$\left(u_{bs}-v_{ps}\right)^2=\tau_{co}^*\frac{\chi aRgD}{\left[1+\tan^2\delta^*\right]^{1/2}}\cos\omega\cos\beta \tag{A25b}$$

where $\chi=\mu/\mu_s$. Now, from (A3c) and (A3d),

$$a\tau=\rho\left|\overrightarrow{u_b}\right|^2\quad\Rightarrow\quad a\tau=\rho(u_{bs}^2+u_{bn}^2)\quad\Rightarrow\quad u_{bs}^2=\frac{a\tau}{\rho}\frac{1}{1+\tan^2\delta} \tag{A26}$$

where

$$\tau\equiv\left|\vec{\tau}\right| \tag{A27}$$

Dividing (A25b) by (A26) we get

$$\left[\frac{u_{bs}-v_{ps}}{u_{bs}}\right]^2=\frac{\tau_{co}^*}{\tau^*}\frac{\left[1+\tan^2\delta\right]}{\left[1+\tan^2\delta^*\right]^{1/2}}\chi\cos\omega\cos\beta \tag{A25c}$$

where

$$\tau^* = \frac{\tau}{\rho RgD} = \frac{\left|\vec{\tau}\right|}{\rho RgD} \tag{A28}$$

(A25c) can be alternatively written as

$$\frac{u_{bs} - v_{ps}}{u_{bs}} = \Gamma^* \sqrt{\frac{\tau^*_{co}}{\tau^*}} \tag{A29a}$$

$$v_{ps} = u_{bs}\left(1 - \Gamma^* \sqrt{\frac{\tau^*_{co}}{\tau^*}}\right) \tag{A29b}$$

where

$$\Gamma^* = \left[\frac{\left[1 + \tan^2\delta\right]}{\left[1 + \tan^2\delta^*\right]^{1/2}} \chi \cos\omega \cos\beta\right]^{1/2} \tag{A30}$$

Reducing between (A29), (A5b), and (A9), we get

$$\tan\delta^* = \tan\delta \frac{1}{\Gamma^*}\sqrt{\frac{\tau^*}{\tau^*_{co}}} - \tan\beta\left(\frac{1}{\Gamma^*}\sqrt{\frac{\tau^*}{\tau^*_{co}}} - 1\right) \tag{A31}$$

Between (23) and (31), then,

$$\tan\beta = \tan\delta - \frac{\chi^{1/2}\Gamma}{\mu}\sqrt{\frac{\tau^*_{co}}{\tau^*}}\tan\varpi \tag{A32}$$

where

$$\Gamma = \frac{\Gamma^*}{\chi^{1/2}\cos\beta} = \left[\frac{\left[1 + \tan^2\delta\right]}{\left[1 + \tan^2\delta^*\right]^{1/2}} \frac{\cos\omega}{\cos\beta}\right]^{1/2} \tag{A33}$$

In the simplified case that $\delta = 0$, (A32) can be rewritten in the form included as Eqn (7) in §3:

$$\tan\beta = -\frac{\left(\frac{\mu}{\mu_S}\right)^{1/2}\left[\frac{\cos\omega}{\left(1+\left(\tan\beta+\frac{1\tan\omega}{\mu\cos\beta}\right)^2\right)^{1/2}\cos\beta}\right]^{1/2}}{\mu}\sqrt{\frac{\tau^*_{c0}}{\tau^*}}\cdot\tan\omega \tag{A34}$$

Appendix B

Description of the Heuristic Avalanche Algorithm

The avalanche algorithm is based on the concepts and experimental results of Allen (1970) and Carrigy (1970), which are described in §2.1. To briefly summarize, the angle of initial yield Φ_i is closely related to the friction angle Φ; experimental observations of Φ_i reflect the phenomenon that under the small time scales of a given slope configuration that is continuously evolving, failure along a failure plane does not occur instantaneously when the factor of safety equals 1; but rather the angle steepens somewhat beyond that before a failure occurs. A small difference between Φ and Φ_i on a concave-up bank profile yields shallow mass failures (avalanches).

Figure B1 references an actual slope configuration at initiation of an avalanche in an example simulation illustrating the procedure used in the avalanche algorithm, which is outlined as follows.

1. The existing ground surface at time t is referred to as "Surface 1". The presence of an instantaneous slope ω that exceeds Φ_i = 40° on Surface 1 initiates the avalanche algorithm. The segment whose slope exceeds the threshold is demarcated "Segment A".
2. Step down the slope from Segment A to search for the computational node defining the interface between instantaneous slope $\omega > \Phi$ and $\omega < \Phi$; this is demarcated as "Node B".
3. Extend a failure plane upslope from Node B at the friction angle Φ until the failure plane intersects Surface 1. The intersection point defines the upper extent of mobilized material and is demarcated "Node C". If there is no intersection point due to the steepness of the upslope region, then the failure plane is projected to the top of the non-cohesive material and Node C is the most upslope node.
4. Calculate the area of the mobilized material which lies between the failure plane and Surface 1. This region is demarcated "AreaMob" and is yellow-shaded.
5. Implement an iterative procedure to determine the configuration of deposited material that is mobilized from upslope.
    a. Start at the first node down-slope of Node B, referred to as Node (B-1). Project a line representing the potential depositional surface upslope at θ_{rm} = 33° until it intersects the failure plane established in Step 3 or until Node C is reached.
        i. If the line does not intersect the failure plane line, then extend the line to Node (C-1) and connect to existing ground elevation at Node C to create a continuous potential depositional surface. Node (C-1) is an inflection point on the potential depositional surface and Node C is the upslope extent of deposition.
        ii. If the line does intersect the failure plane, the intersection location is almost certain to occur between nodes. The downslope node of the segment is set as the upslope extent of deposition with elevation

established per the failure plane. The node immediately downslope forms the inflection point.

b. Calculate the resulting area between the potential depositional surface of Step 5a and the underlying unmobilized surface; this area is referred to as "AreaDep".
c. Compare AreaDep with AreaMob. If AreaDep < AreaMob, then return to Step 5a, move one node further downslope from Node B, and repeat Steps 5a and 5b until AreaDep $\geq$ AreaMob. The first downslope node where AreaDep $\geq$ AreaMob is demarcated as "Node D"; it defines the toe of deposition.
d. It is very unlikely that AreaDep is exactly equal to AreaMob after Step 5c; this means that in reality the toe of deposition lies between Node D and the node just upslope. However, by using a small Δy^*, this error is minimized. To ensure mass conservation, elevations are modified on the upslope nodes of deposition by modifying the location of the inflection point described in Step 5a. Starting at the current location of the inflection point, move one node downslope to establish a new inflection point and linearly interpolate elevations between that node and the node forming the upslope extent of deposition. Recalculate AreaDep, and check if the new AreaDep is equal to AreaMob within a reasonable tolerance. If not, then continue moving the inflection point downslope as described until AreaDep is equal to AreaMob within a reasonable tolerance.

6. The new post-avalanched surface is thus established between Node D and Node C; bank deformation associated with bedload processes can then proceed.

Note that the avalanching process is assumed to occur instantaneously; in other words, once the bedload processes yield a surface having a segment with $\omega > \Phi_i$, then modeling the next time step for bedload processes does not begin until a final post-avalanched surface is generated.

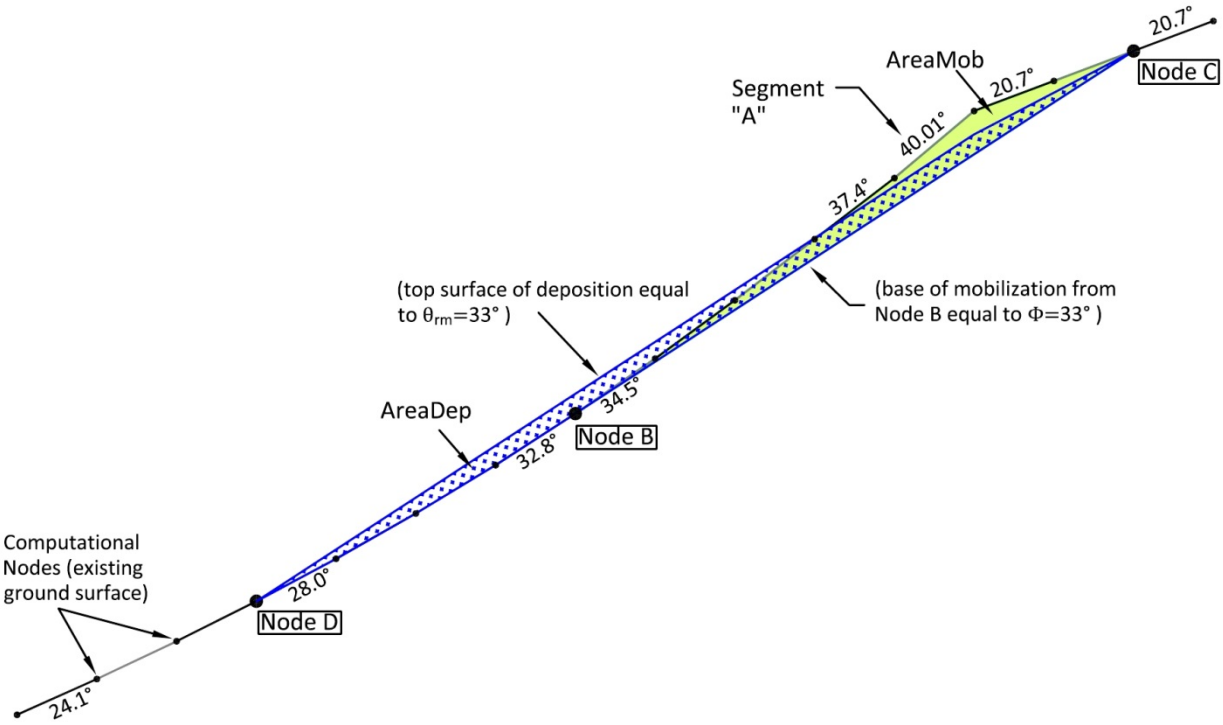

Figure B1: Schematic Cross-Sectional Diagram illustrating the Avalanche Algorithm. The initial ground surface of this simulation was a uniform transverse slope with ω = 20.7°. Just below the $\tau^*/\tau^*_c = 1$ interface, the slope gradually steepened, and eventually ω exceeded Φ_i = 40°; this is the condition illustrated above. AreaMob is calculated in the yellow-shaded region between Node B and Node C. AreaDep = 1.39x AreaMob as shown in the blue cross-hatching; if Node D was at the node just upslope, AreaDep = 0.725x AreaMob. An AreaDep that exceeds AreaMob is a numerical artifact, which is minimized as Δy^* becomes smaller. To ensure mass conservation, the depositional surface must be modified. The modified depositional surface still spans from Node D to Node C but the inflection point near Segment A is moved downslope; the downslope portion of the depositional surface has slope = θ_{rm} and the portion upslope of the inflection point has slope slightly less than θ_{rm}.